

ATTEMPT OF MODELLING THE XMM-NEWTON RADIATION ENVIRONMENT

prepared by/ *préparé par*

M. Casale

J. Fauste

reference/ *référence*

XMM-SOC-OPS-TN-0004

issue/ *édition*

1

revision/ *révision*

0

date of issue/ *date d'édition*

26 January 2004

status/ *état*

Final

Document type/ *type de document*

Technical Note

Distribution/ *distribution*

VILSPA: R. Muñoz, L. Metcalfe, S. Rives, B. Olabarri, G. Buenadicha, N. Cheek, A. Pollock, C. Gabriel, B. Altieri, M. Smith, M. Kirsch, M. Ehle, R. González, P. Rodríguez, M. Santos, L. Tomás, M. Breitfellner, N. Schartel, M. Guainazzi

ESOC: D. Heger, O. Ojanguren, A. Smith

ESTEC: F. Jansen

A P P R O V A L

Title <i>titre</i>	Attempt of modelling the XMM-Newton radiation environment	issue 1 <i>issue</i>	revision 0 <i>revision</i>
-----------------------	---	-------------------------	-------------------------------

author <i>auteur</i>	Mauro Casale	date 26 January <i>date</i> 2004
-------------------------	--------------	-------------------------------------

approved by <i>approuvé by</i>	Mauro Casale.	date 26 January <i>date</i> 2004
-----------------------------------	---------------	-------------------------------------

C H A N G E L O G

reason for change / <i>raison du changement</i>	issue / <i>issue</i>	revision / <i>revision</i>	date / <i>date</i>

C H A N G E R E C O R D

Issue: 1 Revision: 0

reason for change / <i>raison du changement</i>	page(s) / <i>page(s)</i>	paragraph(s) / <i>paragraph(s)</i>

T A B L E O F C O N T E N T S

1	REFERENCES	4
2	INTRODUCTION	5
3	SCOPE OF THE MODEL	7
4	ANALYSIS OF PAST DATA AND KEY ELEMENTS FOR AN XMM RADIATION MODEL	10
4.1	Preliminary Considerations	11
4.1.1	Why do we see a seasonal trend ?.....	11
4.1.2	Why do we observe a noisy trend ?	17
5	ATTEMPTS TO EXPLAIN THE XMM RADIATION DATA with EXISTING RADIATION MODELS	21
5.1	The NASA AE8/AP8 models	21
5.2	The CRRESELE/CRRESPRO (ECM97) models.....	23
6	ALTERNATIVE APPROACHES	25
7	A GEOMETRICAL EMPIRICAL RADIATION MODEL	27
7.1	Key elements for the definition of the surface	27
7.1.1	Selection of the reference system	27
7.1.2	Rad_Mon real data projected in the SM system.....	29
7.1.3	Basic concept for defining the “radiation surface”	33
7.2	Determination of “radiation surface” size and shape.....	34
7.2.1	How to get some hints about the surface size.....	34
7.2.2	How to get some hints about the surface shape.....	38
7.3	Final equations and model results.....	42
7.3.1	Mathematical equations.....	42
7.3.2	Model results	42
7.3.3	Model algorithm	49
7.3.4	Model outcomes.....	50
7.3.5	Model predictions (next 90 revolutions).....	57
	ACKNOWLEDGMENTS	59

1 REFERENCES

RD-1: SPENVIS web page and documentation:

www.spenvis.oma.be/spenvis/help/background/magfield/bl.html

RD-2: lotus note from Mr. H. Evans on 23/10/02 “XMM RM data”

RD-3: Introduction to the space environment PH2514 by R.C. Olsen –January 2003

RD-4: TREND documentation

2 INTRODUCTION

Since the beginning of the XMM-Newton mission the radiation environment has always constituted a threat for the scientific instruments and measures have been taken to protect the instruments against potential damages. A history of the various strategies adopted since launch is provided here below:

- **At launch:**
 - monitoring of radiation based on **Radiation Monitor (RM) only** (Warning Flag parameter M5012 for both MOS's & PN)
 - thresholds: 100 cps for both LE0 & HE0 channels
- **End of January 2000:**
 - RM thresholds were lowered to 30 cps for both LE0 & HE0
- **Beginning of February 2000:**
 - RM thresholds were further lowered to 10 cps for LE0 (HE0 remains to 30cps) in the attempt of detecting “low energy protons events”
- **March 2000:**
 - monitoring based on **RM only** (WF parameter M5012 for MOS's, WF parameter MD027 for EPIC-PN) in order to decouple MOS (more sensitive to radiation) and PN
 - thresholds for MD027: 50 cps for LE0, 20 cps for HE0; as before for M5012
- **June 2000:**
 - monitoring based on **RM & RGS radiation parameters**
 - RM thresholds increased by 40 % for both M5012 (MOS's) and MD027 (PN) i.e.: LE0 MOS : 14 cps, HE0 MOS: 42 cps; LE0 PN : 70 cps, HE0 PN: 28 cps;
 - RGS parameters (R1SUD9, L1SUD9) for detection of low energy protons (requires RGS in Spectroscopy mode) were added.
 - new Radiation parameters for EPIC's were defined, i.e.: for EPIC-PN based on Discarded Line TM, for EPIC-MOS based on sum of count rates from peripheral CCD's
- **End of August 2000:**
 - monitoring based on **RM & RGS radiation parameters**
 - the RGS parameters R1SUD9, L1SUD9 were replaced by derived parameters (GDS005, LDS005) executing a running average over 2 minutes for spike filtering

- **Mid September 2000:**

- monitoring based on **RM and RGS, MOS & PN radiation parameters**
- after the RGS-1 CCD-7 failure and subsequent change in RGS operational strategy a check on MOS and PN parameters was introduced to complement the RGS TM

- **October 2000:** redefinition of the radiation strategy based on the following principles:

- the limits previously applied on RM outputs were over-conservative (waste of science time) and unnecessary (since low energy protons could not be detected anyhow)
- the RM information shall mainly be used to detect entry/exit into/from the Earth radiation belts and “big” solar flares. Low energy proton events along a revolution can on the other hand be detected from information provided directly by the instruments (MOS, PN, RGS detector data). A full set of DP’s have been implemented for this purpose (see above).
- PN is much more robust than MOS and needs less stringent criteria
- RGS needs to be “saved” as well (transition to SETUP mode), while crossing the radiation belts and in case of “big flare”.

The implementation based on above concepts has been successfully in use up to date and can be summarized as follows:

- RM thresholds at 500 cps for detection of **radiation belts around Perigee** and “**big**” flares only
- If RM WF = ACTIVE, then EPIC’s are closed, RGS commanded to SETUP mode
- Protection against low energy protons is implemented as follows:
 - **MOS:** MOS info based on counts on peripheral CCD’s (EDS001, KDS001)
PN info based on Discarded line and limit set to 250, 800, 2400 (FD103)
RGS info based on CCD-9 TM and limit set to 80 (GDS005, LDS005)
 - **PN:** PN info based on Discarded line and limit set to 400, 1200, 3200 (FD131)
RGS info based on CCD-9 TM and limit set to 230 (GDS007, LDS007)

3 SCOPE OF THE MODEL

As indicated in the previous paragraph, the Radiation Monitor outputs play an important role in determining the entry and exit into/from the Earth radiation belts. The limit currently in use is 500 cps; this was determined from experience and it has proved to work very satisfactorily for the safeguard of the instrument integrity. The start and stop of science activities is strictly linked to the Radiation Monitor information, i.e. Warning Flag = INACTIVE means “green light” for the start of science (post-perigee situation), while Warning Flag = ACTIVE means that science activities have to be terminated (pre-perigee situation).

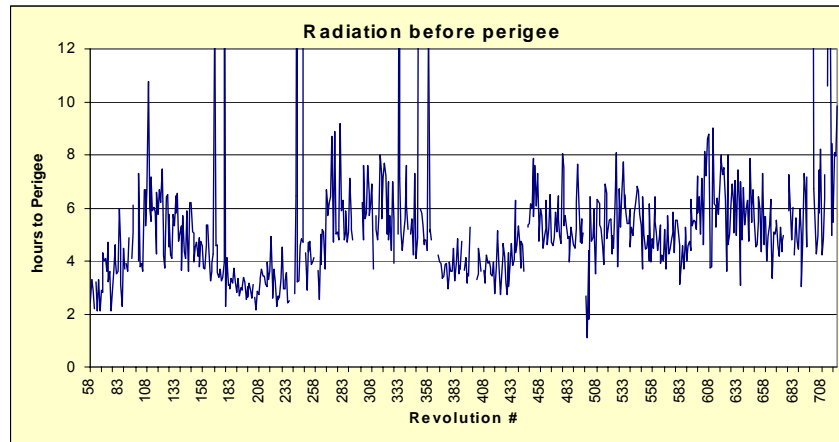


Fig 1: time at which the transition of the WF to ACTIVE took place during the XMM mission (Rev-58 to 720)

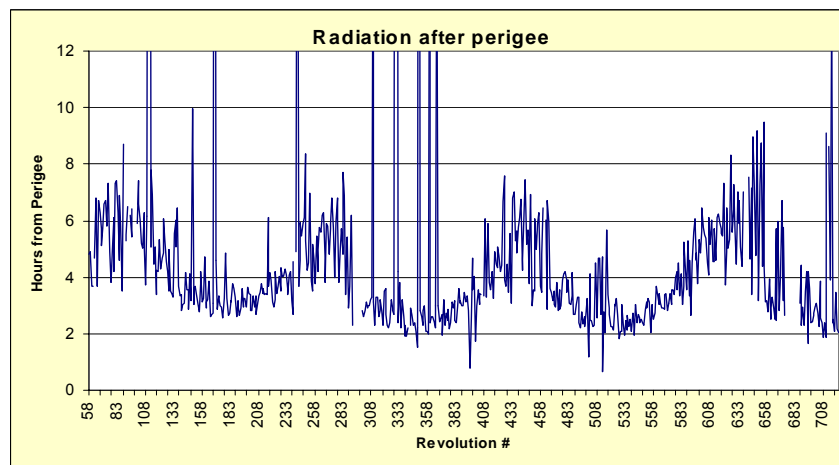


Fig 2: time at which the transition of the WF to INACTIVE took place during the XMM mission (Rev-58 to 720)

The time when the radiation monitor becomes ACTIVE before perigee (expressed in number of hours to perigee) is presented in fig. 1 from Revolution 58 (start of CPV phase) until REV-720 (mid November 2003). Fig. 2 shows on the contrary the time when the radiation monitor warning flag becomes INACTIVE after perigee (expressed in number of hours from perigee), for the same period of the mission.

The “big spikes” extending over 12 h represent solar flares, where a large portion or even the totality of the revolution was affected by high radiation level. The total time required for crossing the radiation belts is shown in fig. 3 (where solar flares have been filtered).

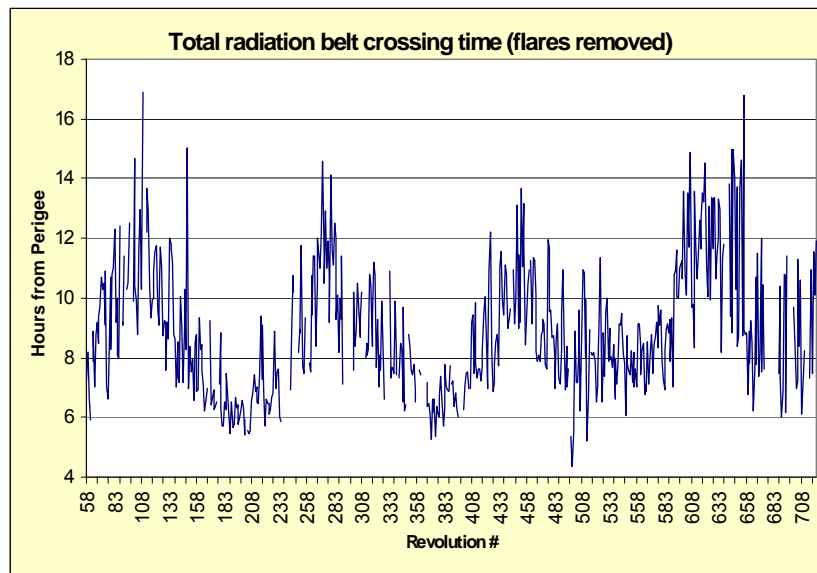


Fig 3: total time required for crossing the radiation belts during the XMM mission (Rev-58 to 720)

By looking at the data after perigee we can see that there are periods along the year where the radiation monitor becomes INACTIVE between 2 to 4 h after perigee, and other periods when this happens between 6 and 8 hours after perigee. In order to compensate for these seasonal variations, in the first part of the mission (until Sept 2003) a calibration observation (with FW in close_cal position for the EPIC instruments) was inserted between 4 h and 6 h after perigee, acting as a filler. This strategy had the advantage that during the “high” radiation period, the time between perigee + 4 h and perigee + 6 h that could not be used for science was utilized to collect calibration data (e.g. for the estimate of CTE degradation). On the other hand during the “low” radiation period, this is time actually subtracted to science. As far as the pre-perigee part is concerned, observations are instead systematically scheduled until perigee – 4 h and then manually terminated when the radiation monitor warning flag reads “ACTIVE”. This optimises the science time but on the other hand potentially reduces the fraction of fully successful observations. In September 2003 the following strategy was adopted: observations start either at

Perigee + 4 h (low radiation periods) or at Perigee + 7 h (high radiation periods); see fig 4 for a visualization. Disadvantages are:

- intermediate situations are not considered (square wave approximation)
- the estimate of when to switch from “good” to “bad” radiation conditions is just based on extrapolation of past data into the future, without actually taking into account dynamical aspects (e.g. orbit evolution)

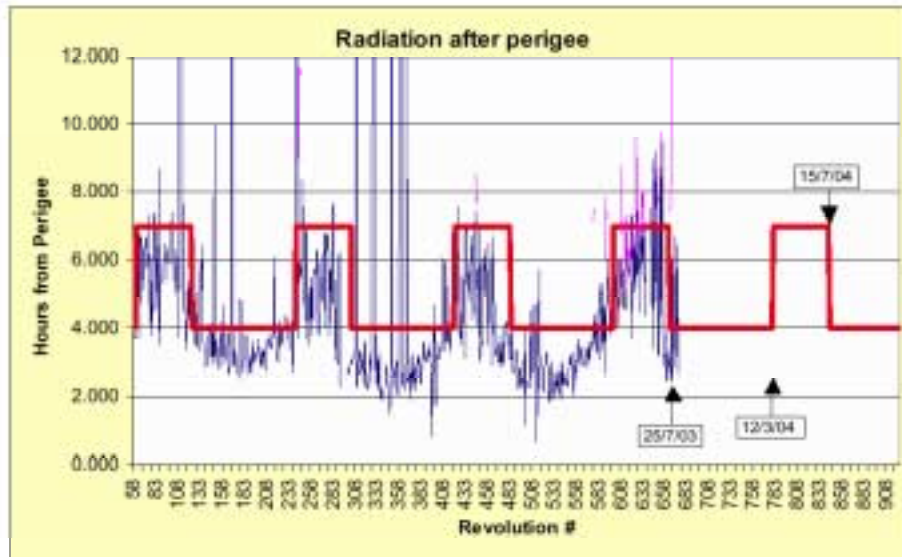


Figure 4 – Radiation level after perigee exit and a simple model for starting the scientific observations

The aim of this TN is to present the work that has been done in the attempt of developing a more satisfactory radiation model which major purposes would be:

- interpret and explain the past data
- predict future behaviour taking into account the Orbit evolution

The final goals of such a model would be to help the Mission Planning process by:

- achieving a higher fraction of successful observations
- slightly increasing the amount of available science time.

For what explained here above, since the model is expected to predict the times when the Warning Flag will become ACTIVE/INACTIVE (based on the RM threshold currently in use) it is also important to notice that:

- the prediction of the radiation spectrum as seen by the Radiation Monitor is outside the scope of the model
- the prediction of the actual count rate (when > or < 500 cps) is not essential, since the only critical information is when this transition occurs.

4 ANALYSIS OF PAST DATA AND KEY ELEMENTS FOR AN XMM RADIATION MODEL

By analyzing the behavior of the radiation environment, as shown in Fig 1 & 2 above, the following observations can be made:

- For the **OUTBOUND leg (i.e. coming out from perigee)** there is a clear **seasonal effect with a period of roughly one year** which consists in the following:
 - the maximum of radiation along the year is reached around the Summer Solstice
 - the minimum of radiation is present around the Winter Solstice
 - the periods corresponding to the Equinoxes (Spring / Autumn) constitute intermediate situations where the radiation environment is very similar (decreasing towards a minimum in Autumn and increasing towards a maximum in Spring, respectively)

This seasonal effect, with a period of about 1 year, is even more evident when looking at the total radiation belt crossing time (see fig 3)..

- For the **INBOUND leg (i.e. going into perigee)** the seasonal effect is quite evident in the first 370 revolutions approximately, then some other conditions have intervened which have somehow broken or made less evident the previous periodicity. This is, as it will be shown later-on, related to the orbit evolution, but its interpretation is not immediate.
- Though a trend for both the INBOUND/OUTBOUND legs can be clearly identified, the data show significant variations already at revolution level, i.e. the curves depicted in fig 1,2,3 look very spiky and **even in the absence of real solar flares, the observed variation between two consecutive revolutions can be as high as 2 h.**

4.1 Preliminary Considerations

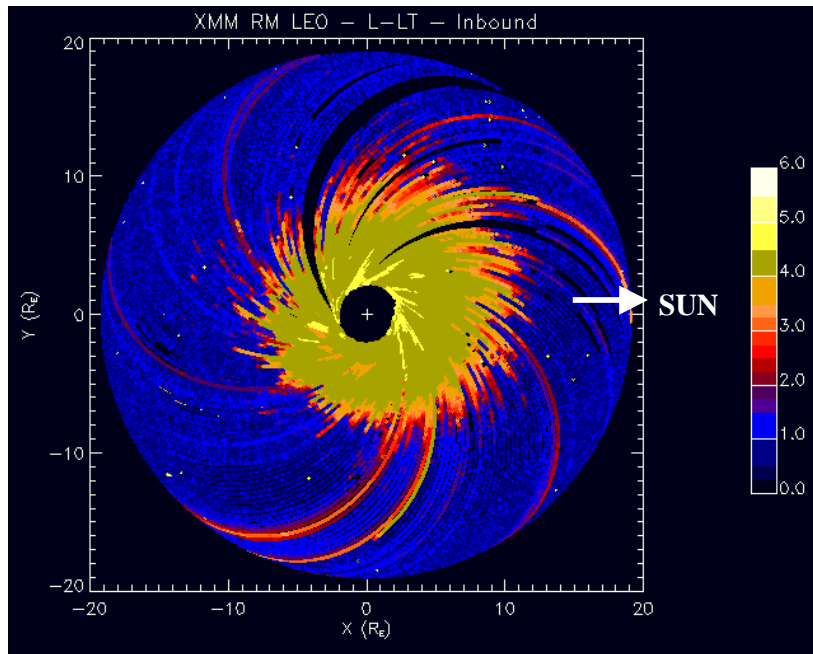
4.1.1 Why do we see a seasonal trend ?

An other way of showing the radiation Monitor data is presented in fig. 5 for both the outbound and inbound legs. These plots were provided in October 2002 by Mr. H. Evans (ESTEC-TOS-EMA); they show the radiation level seen by the radiation Monitor in a pseudo-magnetic field coordinate "L" (i.e. McIlwain's parameter expressed in Earth radii) and local time. The noon side is to the right and the night is to the left. As it can be seen, the radiation belts extend further to the noon side than the night side, i.e. there is an asymmetry between the sunward direction and the anti-sun direction as far as the size of the radiation belt is concerned. This is a consequence of the asymmetry of the actual Earth magnetic field (see fig 6, 7 & 8) when the interaction with the solar wind is taken into account. As visualized in fig. 6 and 8, the simple dipolar model with perfect symmetry around the dipole axis has to be replaced by a more complex model which requires a dependency on the azimuth too, in addition to distance and latitude (see Tsyganenko model).

Taking into account the asymmetry of the Earth magnetic field along the sunward-antisun line, which implies a similar asymmetry on the extension of the radiation belts, and considering the Earth-Spacecraft-Sun geometry at perigee in the two cases of Winter and Summer solstice respectively (see fig 9A and 9B obtained from the CLUSTER OVT tool customized with the XMM Orbit File), it appears clear that:

- crossing the radiation belts in Summer takes significantly longer than in Winter (see fig. 9C for a visualization). This is perfectly in line with the observed seasonal behavior.
- The period of the seasonal trend must be about one year (i.e. amount of time which takes to reproduce the same Earth-Sun-XMM perigee geometry).

Inbound legs



Outbound legs

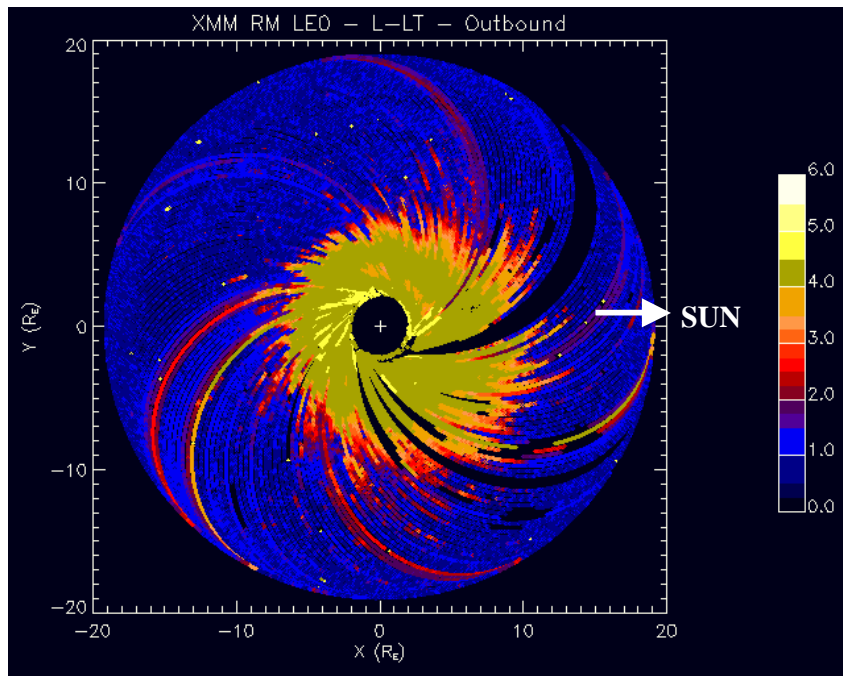


Figure 5 – RM data represented in L-UT coordinates

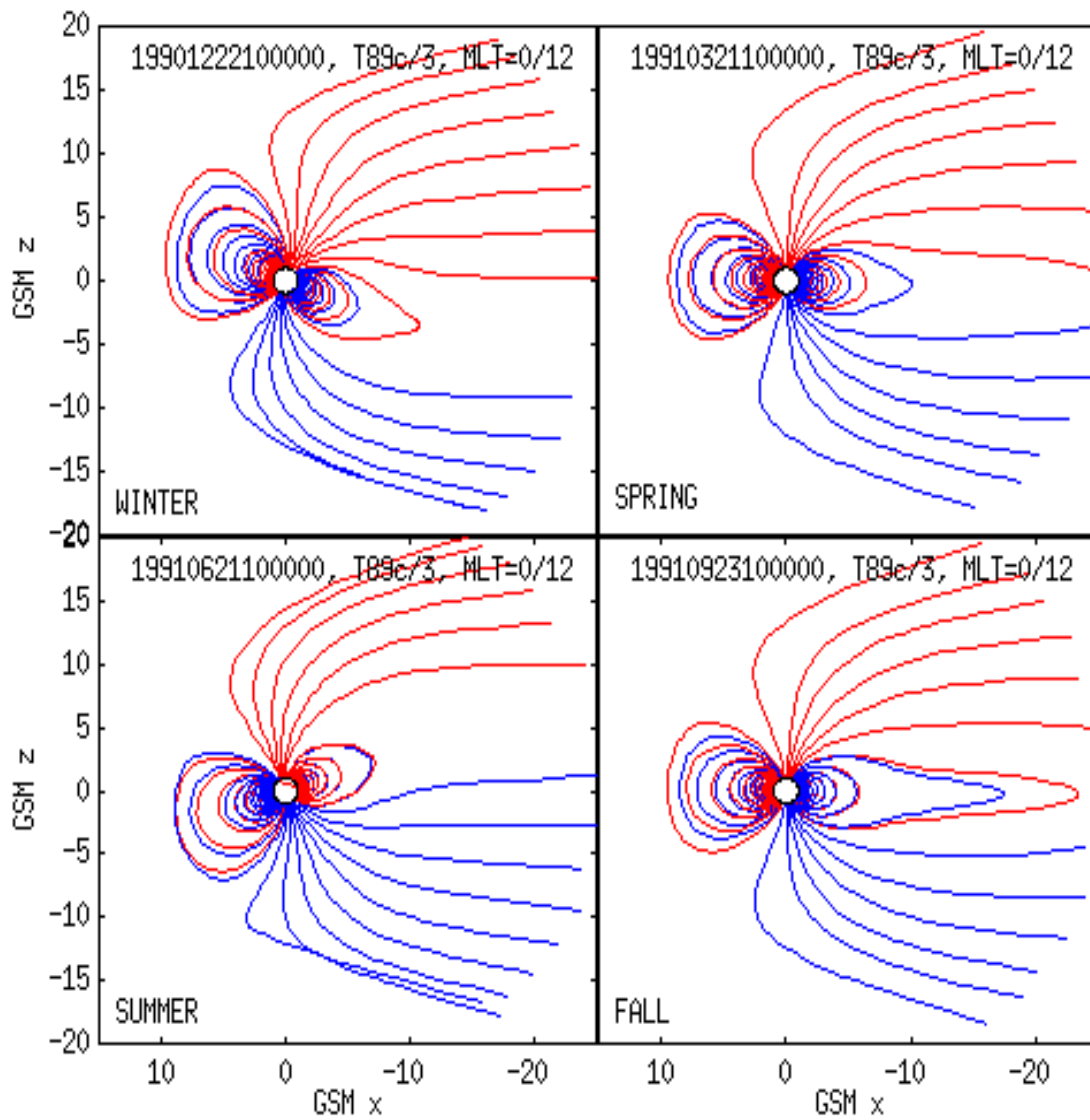


Figure 6 – Earth magnetic field measurements (for different seasons) in the GSM system

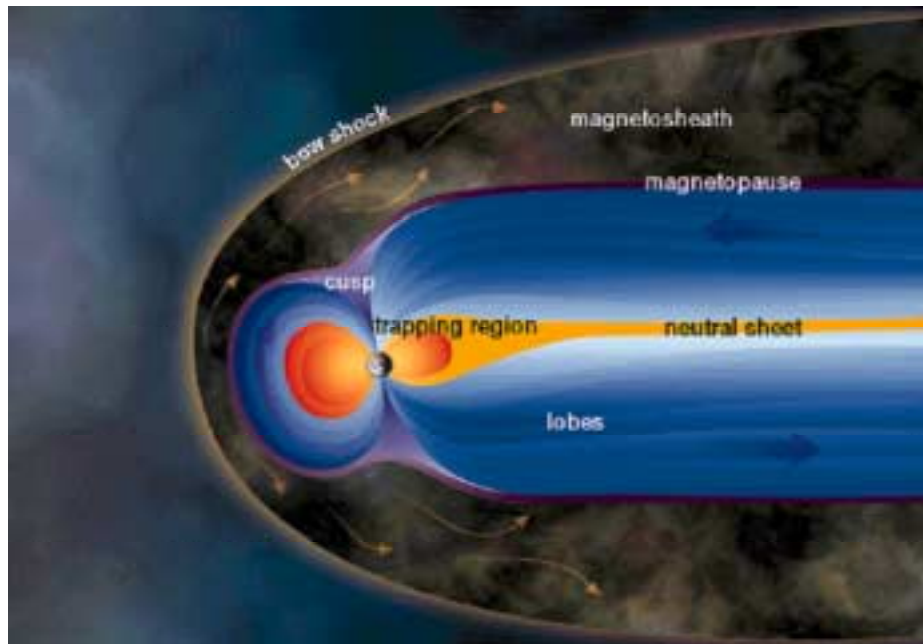


Figure 7 – Earth magnetic field pictorial representation (I)

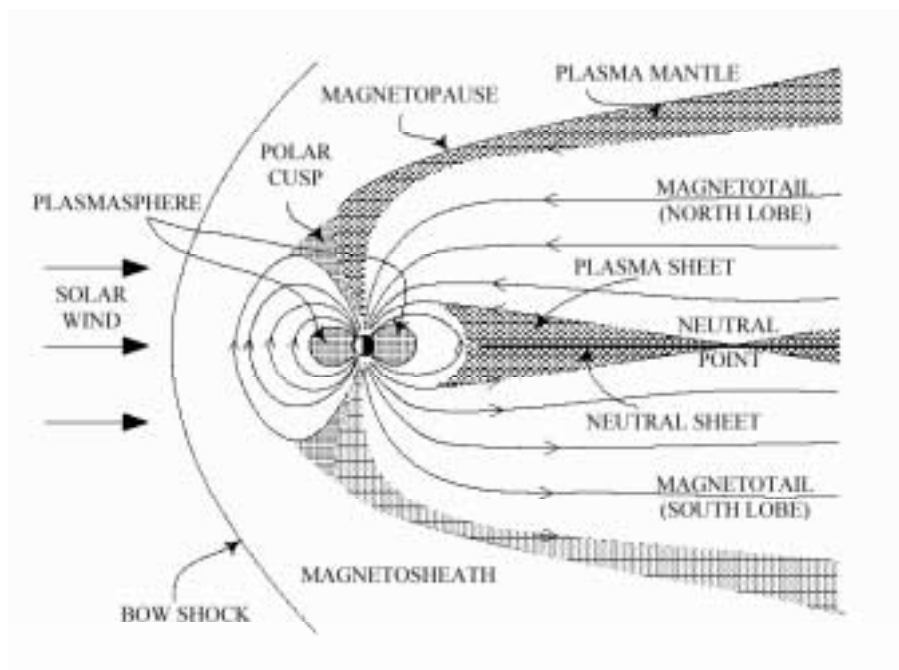


Figure 8 – Earth magnetic field pictorial representation (II)

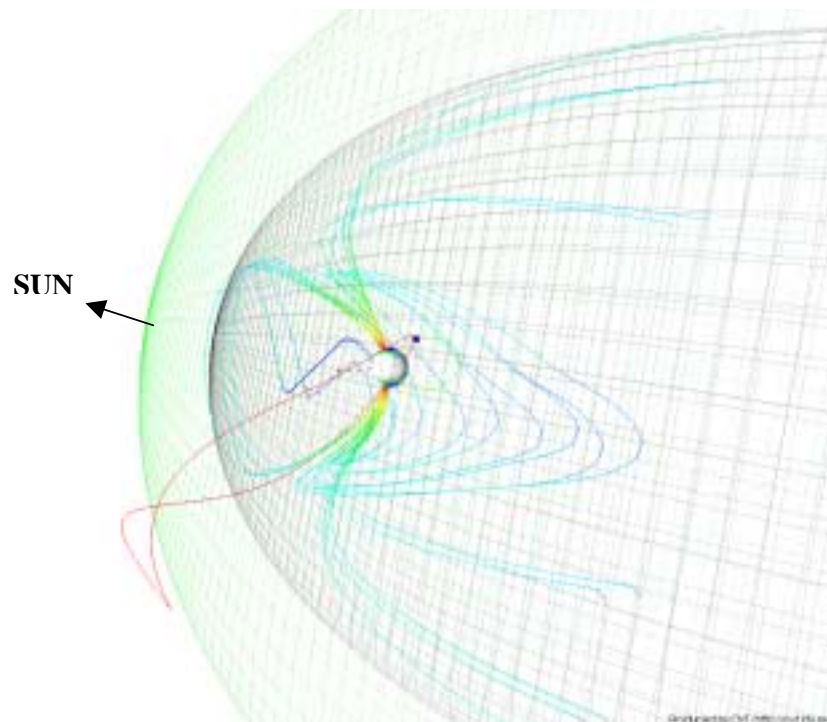


Figure 9-A – perigee position for Rev-464 (Summer solstice of year 2002) in the SM reference system (see paragraph 7.1.1 for a definition)

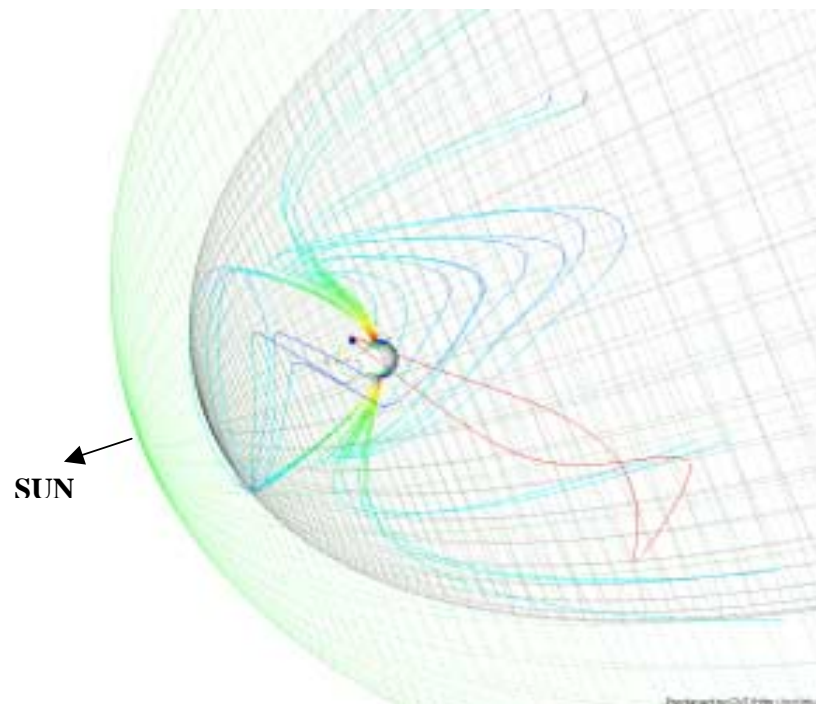
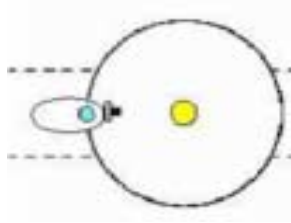


Figure 9-B – perigee position for Rev-374 (Winter solstice of year 2001) in the SM reference system (see paragraph 7.1.1 for a definition)

Winter solstice



Summer solstice

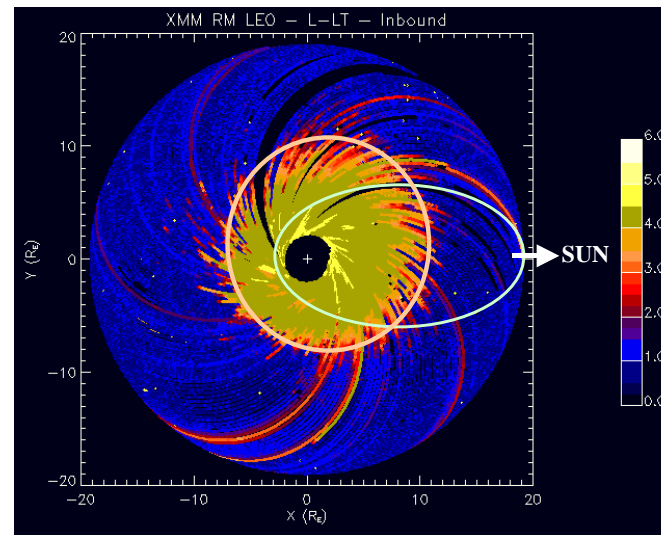
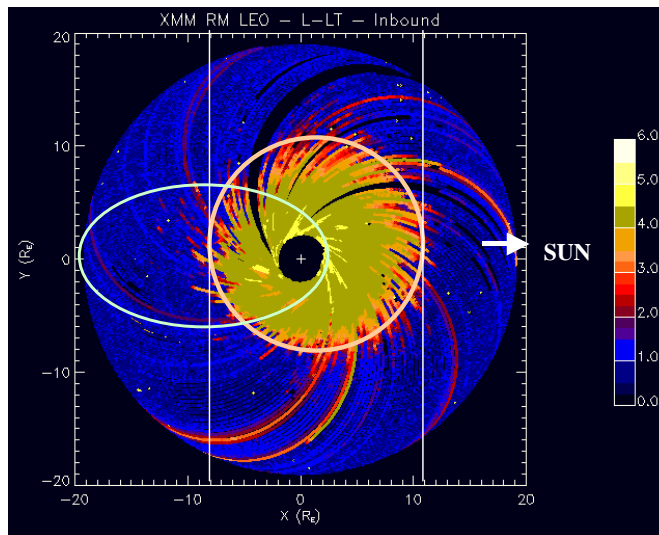
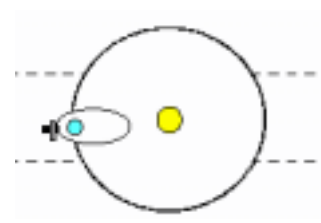


Figure 9-C – radiation belts crossing at Winter and Summer solstices

4.1.2 Why do we observe a noisy trend ?

The “spiky behaviour” (see fig 1 and 2) must certainly be linked to high frequency (hourly or diurnal) variations of the radiation belts induced by changes in the geo-magnetic environment. These are normally measured in terms of geo-magnetic indexes: the most popular ones are the Ap and Kp indexes. The Ap index (as the equivalent Kp index) is a measure of the general level of geomagnetic activity over the globe for a given day. It is derived from measurements made at a number of stations world-wide of the variation of the geomagnetic field due to currents flowing in the Earth's ionosphere and, to a lesser extent, in the Earth's magnetosphere. The evolution of the Ap index during the XMM mission is shown in fig.10 (picture at the top).

It can be seen that there is a clear correlation between changes in Ap index and changes in the radiation belt crossing time (spike amplification). This could suggest that the XMM radiation model might include a dependency on Ap (or equivalently Kp, see note at bottom of page) to account for short term variations of the radiation belt crossing time. On the other hand it has to be noticed that the main purpose of the model is to predict the future trend, while information about geo-magnetic index values can only be acquired a posteriori. It is therefore decided that no modelization of the Ap (or Kp) dependency will be incorporated, since it will not add any useful information for predicting the future behavior. In this way we are implicitly making the assumption that, despite disregarding high frequency effects (hours/days) the global mean structure of the radiation belts can be determined. Any model that will be developed with such a baseline will be a static model and will not be able to account for diurnal variation of the radiation environment induced by sudden changes in the space weather. **The expected error on daily basis can therefore be up to a couple of hours, depending on the solar activity intensity.**

Disregarding high frequency effects is equivalent to removing the noise from the curves of fig 1 & 2 and actually work with smoothed curves derived from the former ones. This can be done by using an IDL provided interpolation algorithm (see fig. 11 & 12). From now on in this document, for any model that will be considered, we will always compare w.r.t. the smoothed data shown in fig. 13 & 14.

Note: the Ap index is related to the Kp index according to the following scale:

K	0	1	2	3	4	5	6	7	8	9
A	0	3	7	15	27	48	80	140	240	400

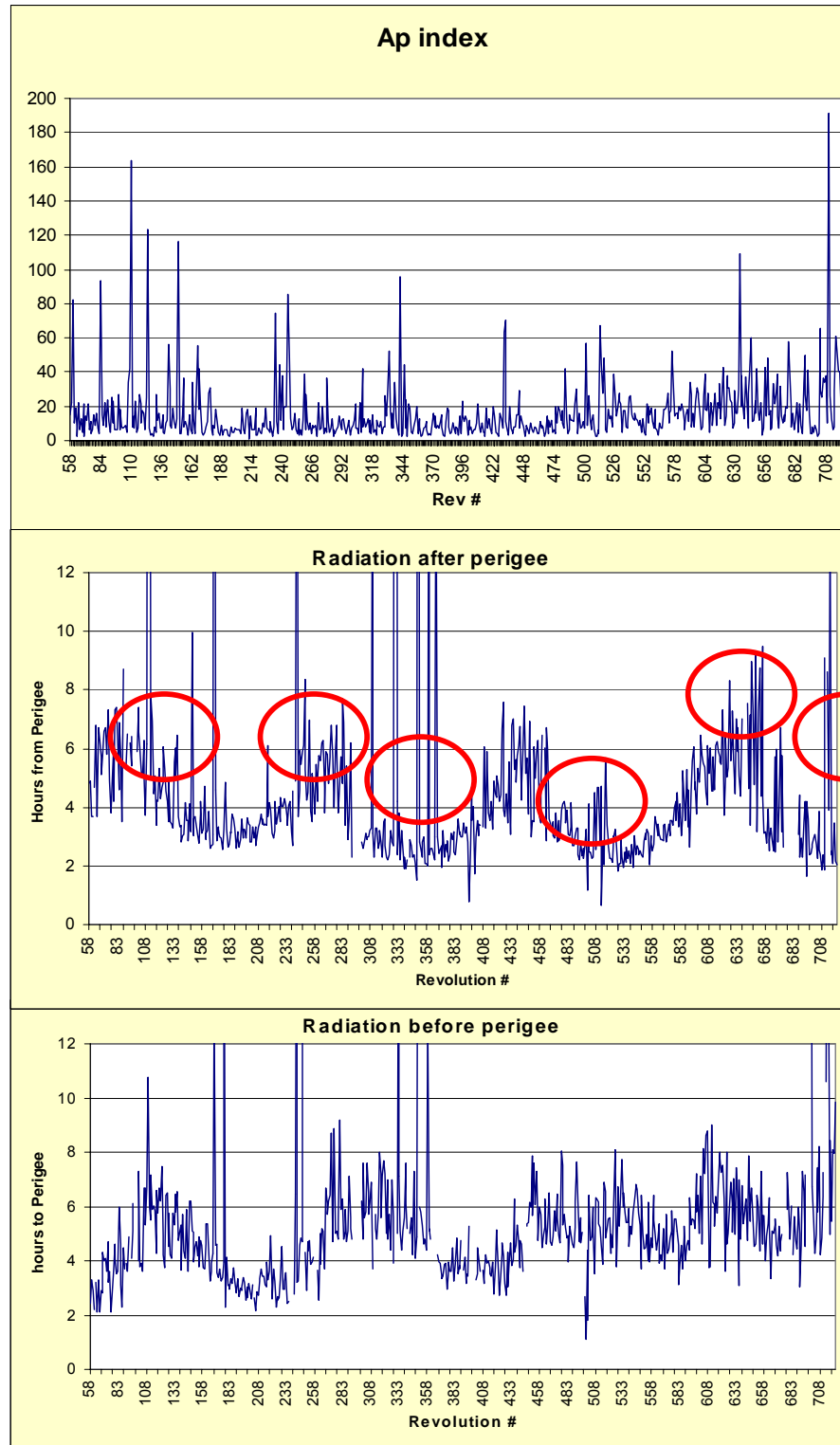


Figure 10 – Correlation between Ap index evolution and Rad_Mon data

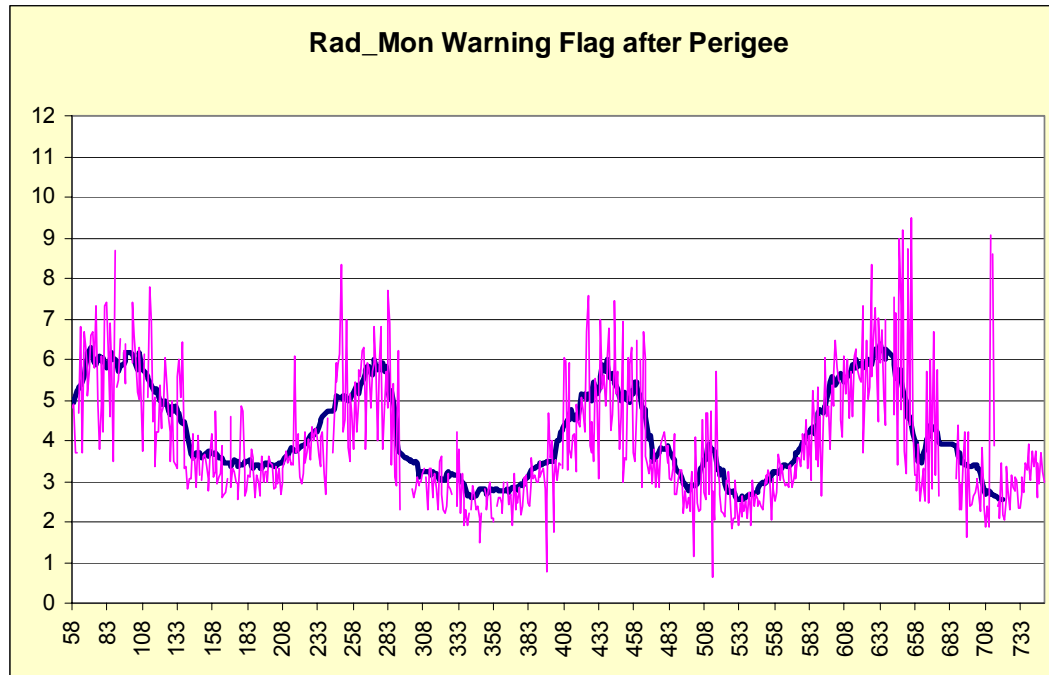


Figure 11 – smooth RM data superimposed to real data (OUTBOUND)

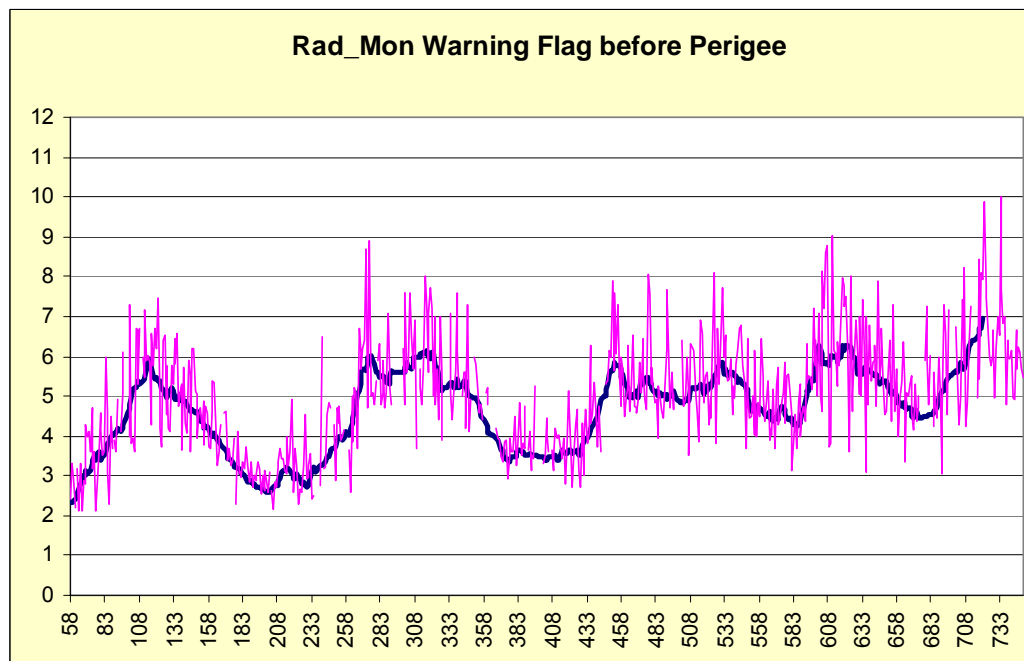


Figure 12 – smooth RM data superimposed to real data (INBOUND)

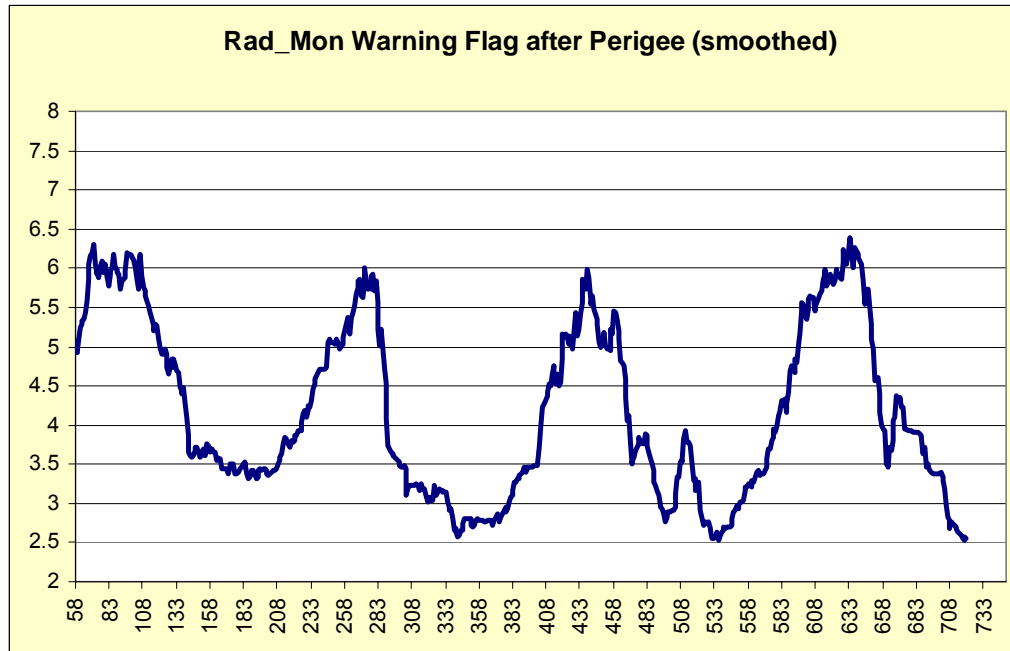


Figure 13 – RM Warning Flag INACTIVE (outbound): smoothed curve

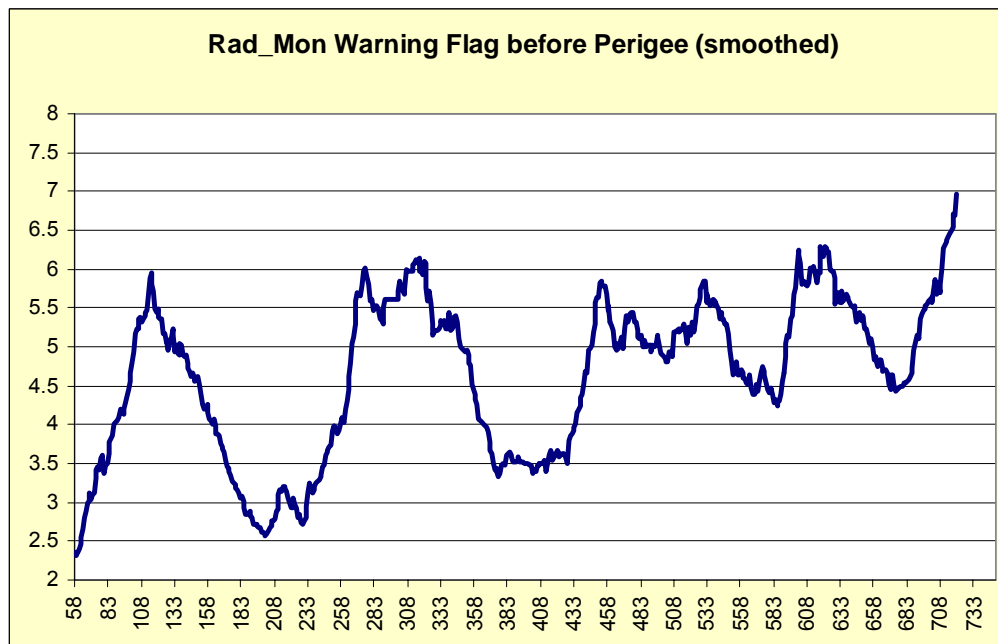


Figure 14 – RM Warning Flag ACTIVE (inbound): smoothed curve

5 ATTEMPTS TO EXPLAIN THE XMM RADIATION DATA WITH EXISTING RADIATION MODELS

Before any trial of developing an independent new model was carried out, several attempts were made to explain the XMM data by using existing radiation models. To this purpose the SPENVIS utility available at:

<http://www.spervis.oma.be/spervis/>

was used. All the models integrated in SPENVIS provide the capability of inserting specific orbit data and predicting the radiation spectrum & count rate along the orbit. By applying the Rad_Mon threshold of 500 cps it would therefore be possible to determine the time during the orbit when the transition to ACTIVE and to INACTIVE take place.

In order to identify whether one of the available models could be used, the following criteria was adopted: as very first and most basic thing that any XMM radiation model should be able to predict and reproduce is the seasonal effect. So all the radiation models that were tried in SPENVIS were tested against the capability (or not) of explaining the seasonal effect. Results of this activity are summarized here below.

5.1 The NASA AE8/AP8 models

The actual output of the XMM Radiation Monitor is shown in fig 15 together with the AE8 and AP8 predictions for the two cases of REV-464 (Summer Solstice of year 2002) and REV-374 (Winter Solstice of year 2001). As it can be seen from the picture, the output of the AE8 (pink and violet) and AP8 model (yellow) is basically the same in the two cases. This means that the AE8/AP8 would predict almost the same time for entry and exit into/from the radiation belts, which is actually in contradiction with the real data. So the AE8/AP8 models can not explain the seasonal behaviour observed in the Rad_Mon data. On the other hand this is not surprising since the AE8/AP8 models were developed in the 60's, when the knowledge about the actual Earth magnetic field structure was not as advanced as now, so a simple dipolar model was used. In other terms this means that the AE8/AP8 models are bi-dimensional (using L as measure of the distance and B, i.e. the magnetic field intensity, as an implicit measure of the latitude); the third coordinate, i.e. the longitude, that would account for the asymmetry between the sunward and anti-sun sides is not considered in the model.

Conclusion: the NASA AE8/AP8 models do not explain the observed XMM radiation data.

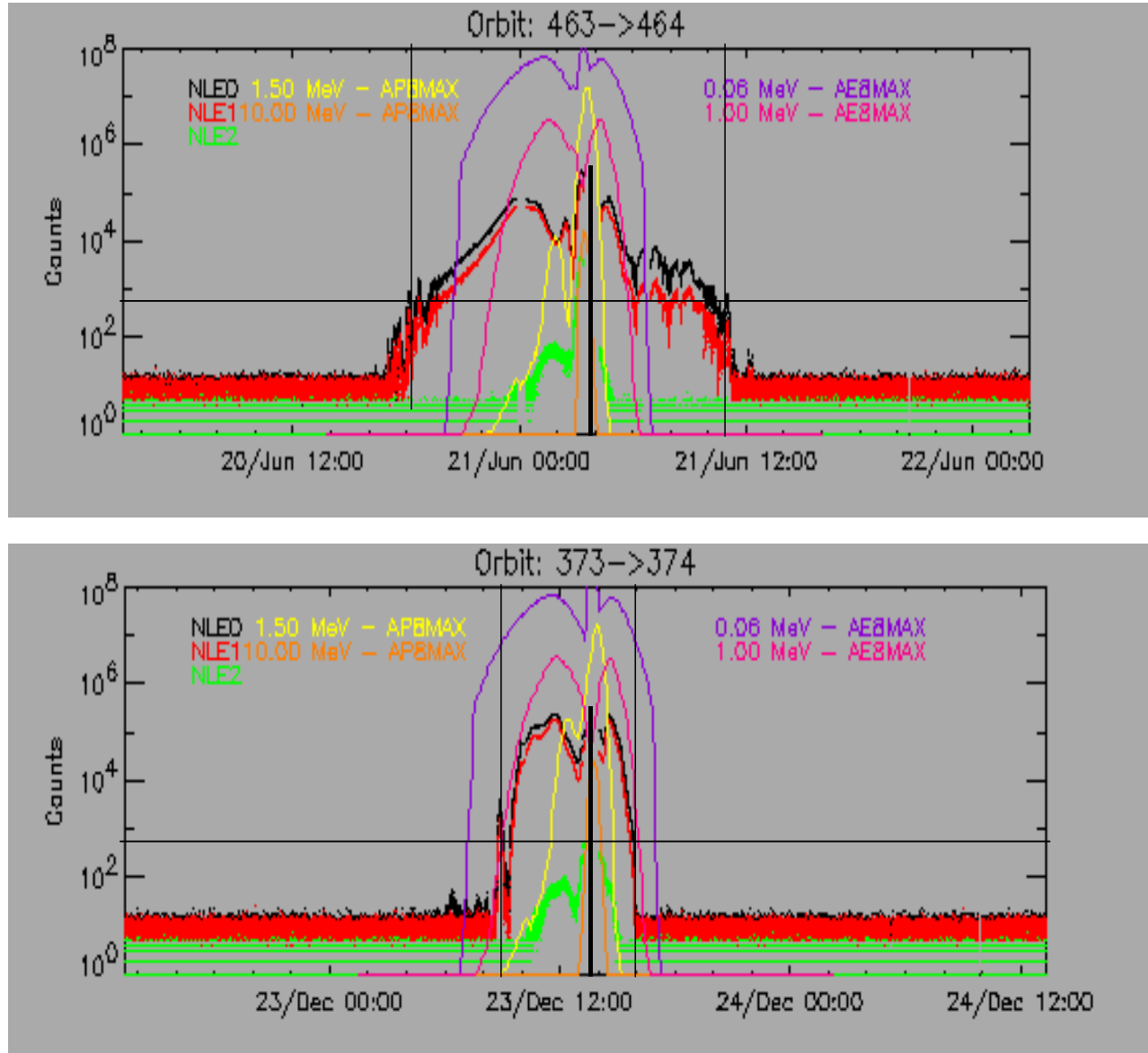


Figure 15 – Comparison of Rad_Mon data with AP8/AE8 predicted outputs

5.2 The CRRESELE/CRRESPRO (ECM97) models

The advantage of this model is that, as clearly seen in fig.16 & 17, it foresees the asymmetry between the sunward-antisun sides which looks quite promising in view of explaining the XMM seasonal effect. Unfortunately the model is limited to 6.8 Earth radii and it therefore does not cover the range of altitudes between 44000 and 65000 Km, where the XMM Rad_Mon warning flag transitions (ACTIVE / INACTIVE and vice-versa) normally take place, independently from the season.

Conclusion: the CRRESELE/CRRESPRO models, though quite promising since based on a three-dimensional magnetic model that could account for the observed seasonal effect, can not be used to interpret the XMM data because limited to altitudes below 44000 Km.

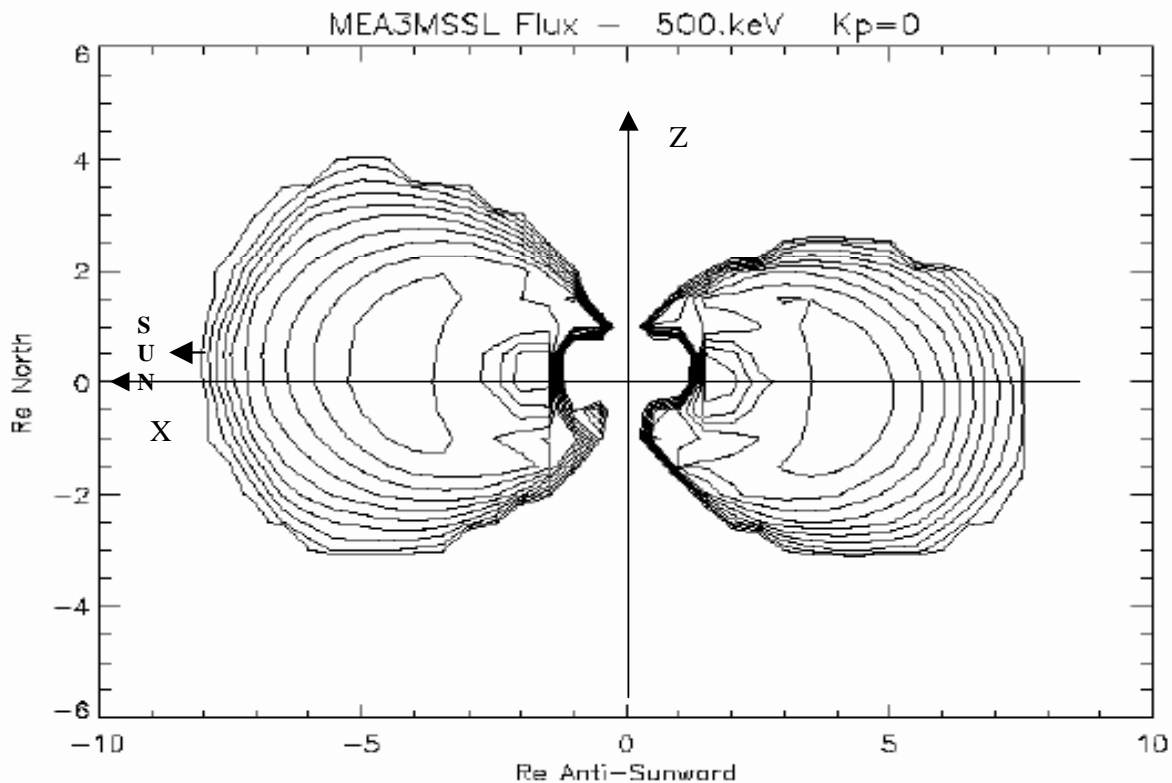


Figure 16 – Contours of logarithmic flux in a noon-midnight cross-section through the magnetosphere at 500 KeV and for Kp = 0 (quiet)

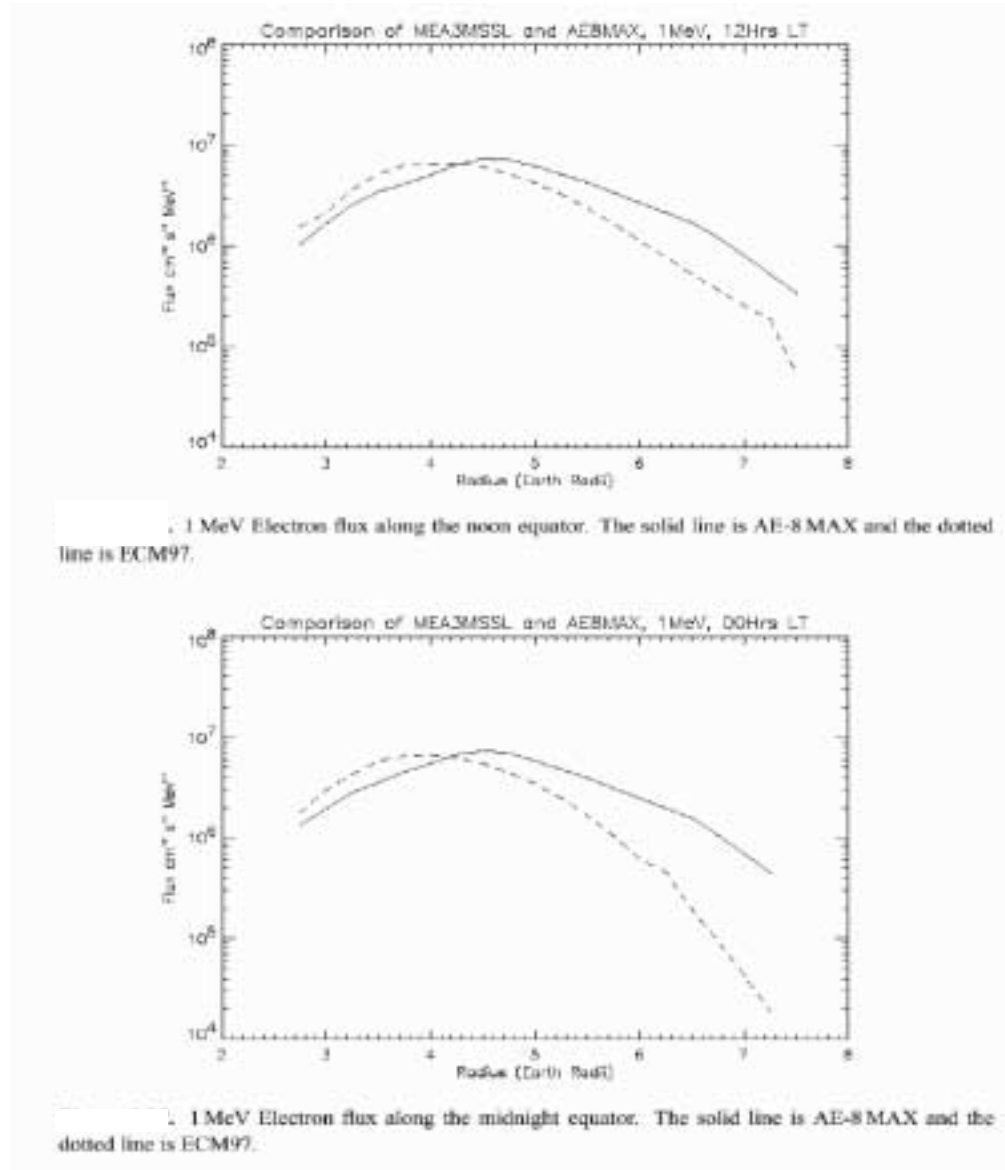


Figure 17 – Flux profiles along the sunward and tailward directions at 1 Mev for NASA AE-8 model and ECM97 model. It can be seen that the peak flux drops off faster with radius in the ECM97 model especially in the tailward (anti-sun) direction. Note that the AE8 model predicts almost no difference between the sunward and tailward sides.

6 ALTERNATIVE APPROACHES

In order to go ahead in the attempt of modelling the XMM radiation environment the following two alternatives can be envisaged:

1) build-up an independent XMM radiation database, by mapping the space around the Earth swept by XMM along its orbit since the beginning of the mission with information of the measured count rate. As indicated above the mapping should be three-dimensional (latitude / longitude / distance) and carried out in an appropriate reference frame (e.g. in Solar Magnetic coordinates, normally referred to as SM reference system). The XMM radiation model would then consists in the following main steps:

- project the XMM orbit for a certain revolution into the chosen reference frame and calculate its position at predefined intervals (e.g. every minute)
- based on the coordinates coming from previous step, access the database and extract relevant count rate information
- compare with threshold and determine whether warning flag is ACTIVE or INACTIVE

Expected difficulties in implementing the XMM radiation database and the subsequent model are:

- The whole activity is expected to be very time consuming (i.e. one FTE or possibly more would need to be devoted full time during several months)
- Filtering algorithms need to be developed to cope with spikes (see paragraph 4.1.2) and to average the data taken in different revolutions at the same spatial coordinates. The choice of these algorithms does not seem to be straightforward.
- The extension of the mapping to regions that have never been crossed by XMM in the past but that could be crossed in the future due to orbit evolution is potentially a rather complex exercise and it is not a priori obvious that a simple interpolation algorithm could work satisfactorily

Based on the above considerations (especially the concern about the effort required) suggested to follow a different route (see below), though the project is not completely ruled out and it could be resumed in the future if deemed necessary and if resources will allow.

2) Geometrical-Empirical approach:

The basic idea consists in representing the Earth radiation environment as an analytical surface surrounding the Earth; in the specific case of XMM the surface envelope would correspond to the threshold currently in use of 500 cps (the parameters defining the size of the surface would of course have to be rescaled in case of change of thresholds). Being inside the surface corresponds to Warning Flag = ACTIVE, while being outside means WF = INACTIVE.

This approach is based on the assumption that, despite disregarding high frequency effects (hours/days) and the local effect of big solar flares, the mean global geometry of the radiation belts can be determined. In addition, it is assumed that the whole radiation belts structure has in average a certain degree of stability to insure the validity of the model (at least in first approximation)

during several years. By following such an approach no information about punctual count rate and radiation spectrum can be provided by the model. As already expressed in paragraph 2, this is anyhow not invalidating the intended usage of the model itself. The developed model, which description will be provided in the following sections, is based on the geometrical-empirical method illustrated here.

7 A GEOMETRICAL EMPIRICAL RADIATION MODEL

7.1 Key elements for the definition of the surface

7.1.1 Selection of the reference system

The first step is the selection of the most suitable reference frame: to this purpose the “Solar Magnetic Coordinates” reference system (normally referred to as SM system) has been chosen.

This is defined as follows:

- the Z-axis is chosen parallel to the north magnetic pole (i.e. aligned with the Earth dipole axis)
- the Y-axis is perpendicular to the Earth-Sun line towards dusk
- the X-axis is contained in the plain identified by the Z-axis and the Sun direction. So the X-axis does not point directly to the Sun; the amount of rotation between the X-axis and the Sun direction is simply the dipole tilt angle.

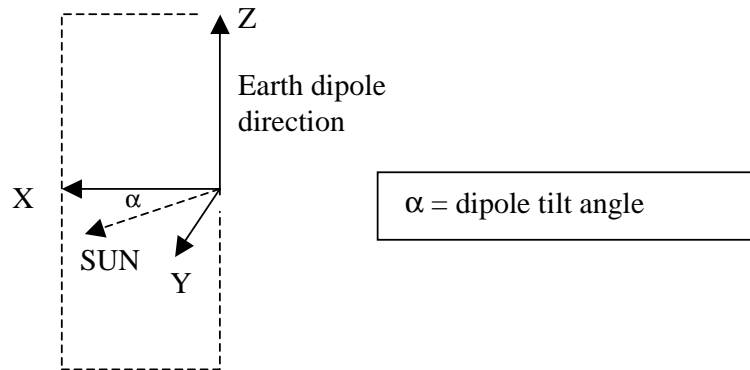


Figure 18 – SM reference system geometry

The X, Y plane is normally identified as the “magnetic equator”.

In the SM reference frame the Magnetic Latitude and Longitude have the following meaning:

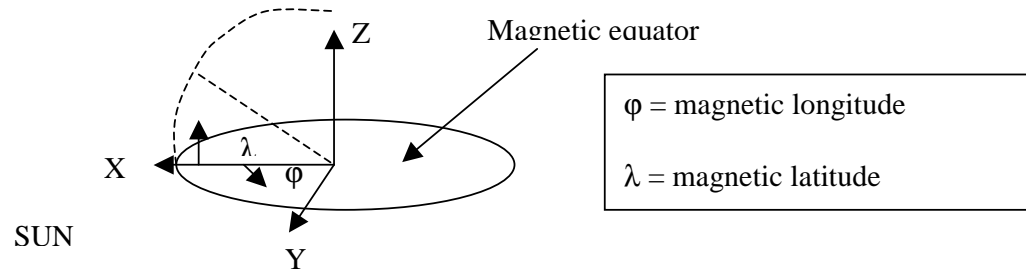


Figure 19 - Visualization of magnetic latitude and longitude in the SM system

The latitude is measured from the magnetic equatorial plane (from 0 to 90 deg for positive Z and from 0 to – 90 deg for negative Z). The longitude is measured anticlockwise in the magnetic equator (i.e. X-Y plane) from the positive X-axis (i.e. from the plane containing the SUN). With this convention the Sun will always be at magnetic longitude = 0 deg, while the anti-sun direction will be identified by magnetic longitude = 180 deg. This is equivalent to say that **in the SM system the Sun is always in the plane +X / Z, and the anti-sun direction is in the plane –X / Z.**

Since the center, orientation and magnitude of the Earth magnetic dipole are not constant, a magnetic field model is required to evaluate them as a function of time; to this purpose the Tsyganenko-2001 model has been used in our algorithms.

It has also to be noticed that the SM system rotates with both a yearly and daily period with respect to inertial coordinates. The transformation from the Inertial reference frame to the SM system is executed in steps:

- convert from GEI (Geocentric Equatorial Inertial system) into GSE (Geocentric Solar Ecliptic system)
- convert from GSE to GSM (Geocentric Solar Magnetospheric system)
- convert from GSM to SM

The advantage of such a reference frame is that any structure attached to the magnetic field geometry and linked to it will appear as static.

7.1.2 Rad_Mon real data projected in the SM system

It is now important to establish the terms of comparison for the model that will be developed. In order to do that the following steps were followed:

- from the “smoothed” RAD_MON ACTIVE / INACTIVE times (see fig 13 & 14) determine by using the orbit file the absolute time of the transitions
- from the orbit file determine the position of the spacecraft in the Geocentric Equatorial Inertial system (time is known from previous step)
- transform above coordinates into the SM system.

The X, Y, Z coordinates in the SM system when the warning flag became ACTIVE (INBOUND leg) or INACTIVE (OUTBOUND leg) during the XMM mission (between REV-58 and REV-720) are shown in fig. from 20 to 23 for both the inbound and outbound legs.

Since these coordinates are based on RM smoothed data, they can be seen as the representation of the average radiation envelope surrounding the Earth for which an analytical expression is searched for.

Any analytical model of the “radiation surface” will have to be compared with above real data to prove the goodness of the model itself.

The magnetic longitude and latitude at which the transition to ACTIVE or INACTIVE took place can be easily determined from the X, Y, Z coordinates and they are shown in fig. 24 & 25.

It is interesting to notice from fig. 24 that the entry/exit magnetic latitudes into/from the radiation belts were very similar in approximately the first year of mission; after that the XMM orbit evolved in such a way that we are always entering into the belts at low latitudes ($|\lambda| < 15$ deg) and exiting at high latitudes ($|\lambda| > 35$ deg).

As it will be explained later-on in this document, this accounts for the fact that the amplitude of the maximums and minimums of radiation for the inbound and outbound legs (see fig. 11 & 12) were the same with almost perfect symmetry (i.e. $\max \approx 6$ h, $\min \approx 3$ h) only during the first year of mission; after that the inbound leg has been in average systematically longer than the exit path.

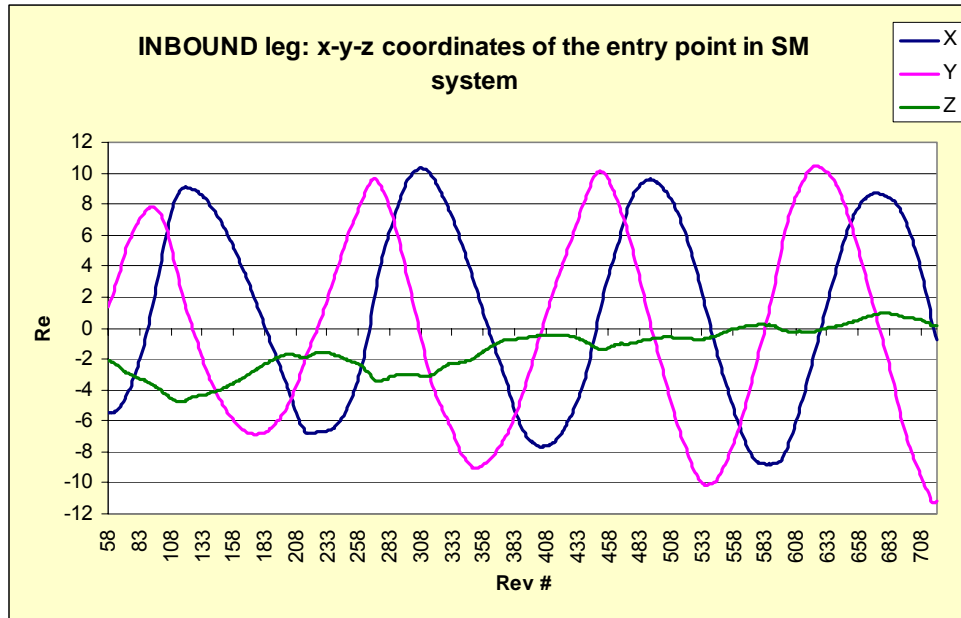


Figure 20 – INBOUND leg: X-Y-Z-coordinates in SM system evaluated from real RM data

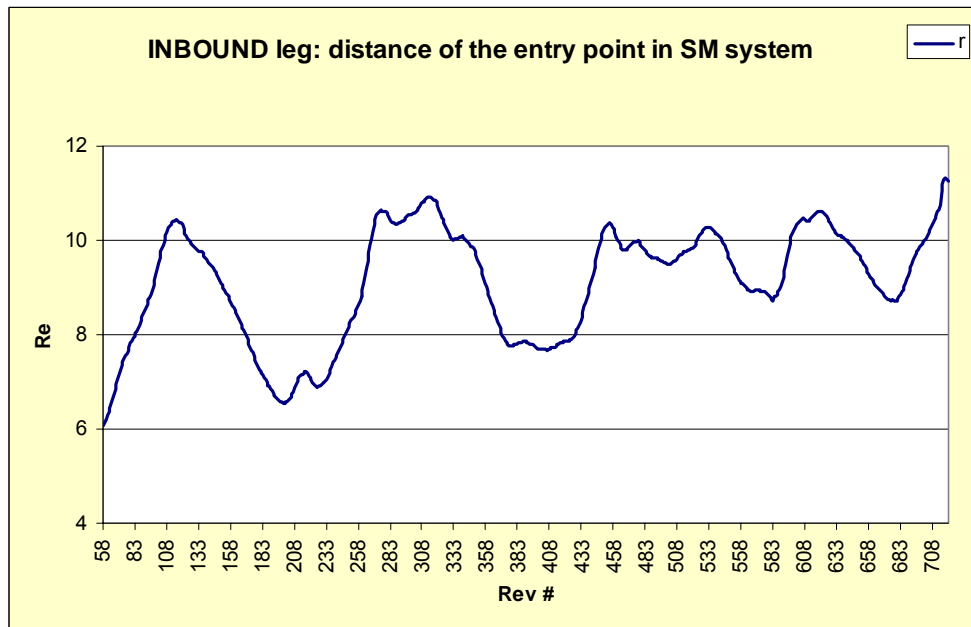


Figure 21 – INBOUND leg: distance evaluated from real RM data

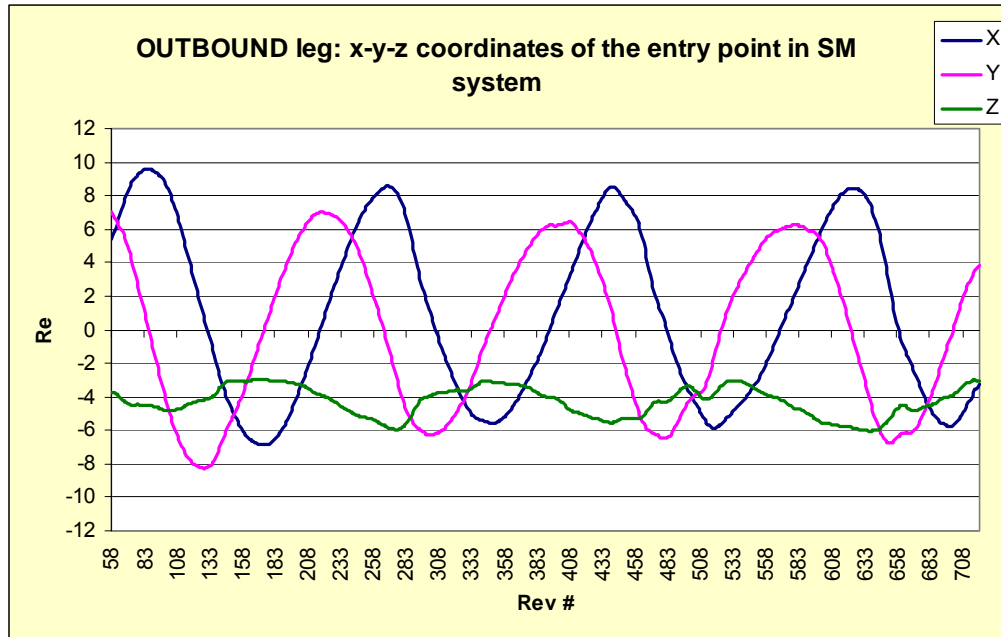


Figure 22 – OUTBOUND leg: X-Y-Z-coordinates in SM system evaluated from real RM data

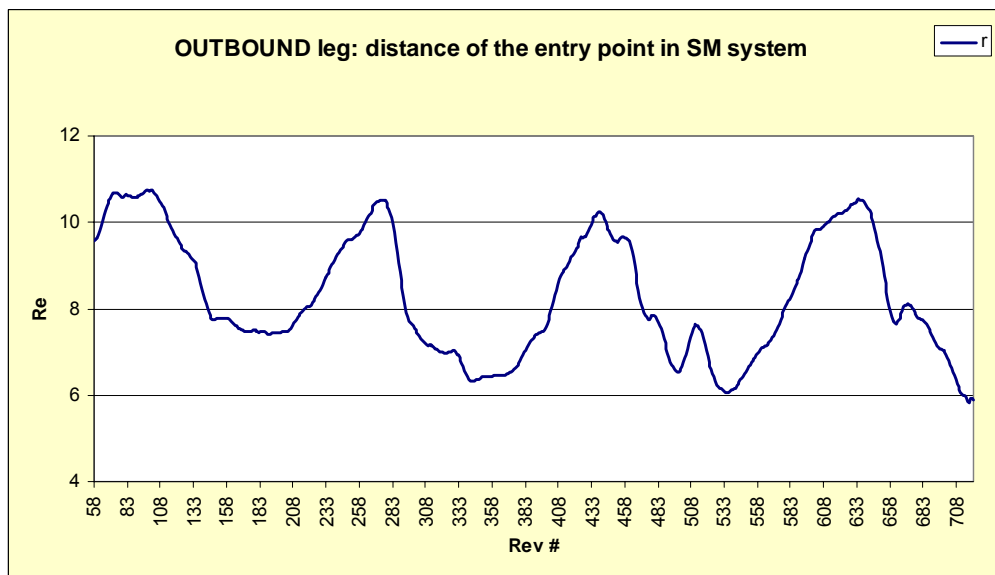


Figure 23 – OUTBOUND leg: distance evaluated from real RM data

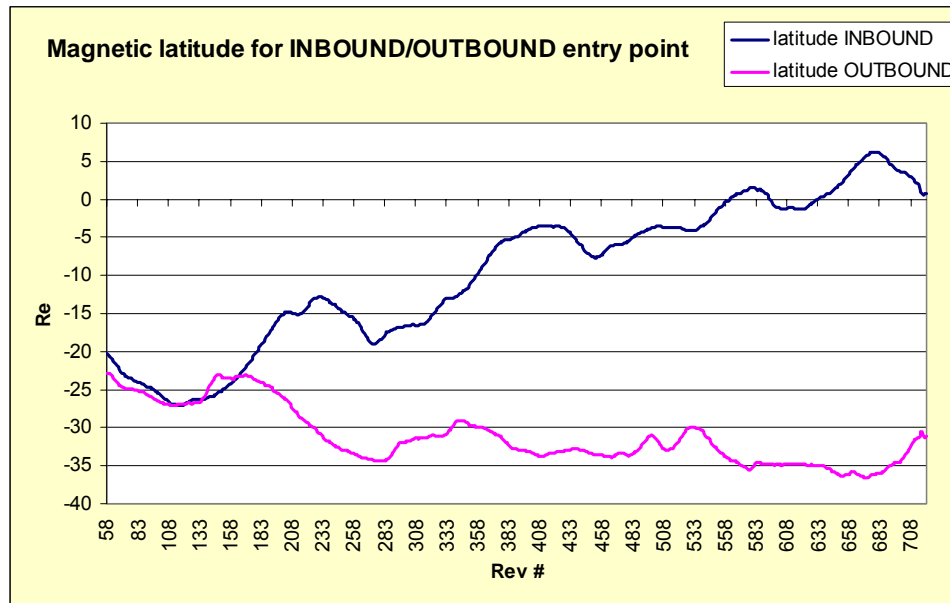


Figure 24 – magnetic latitude (SM system) evaluated from real RM data for both INBOUND and OUTBOUND legs

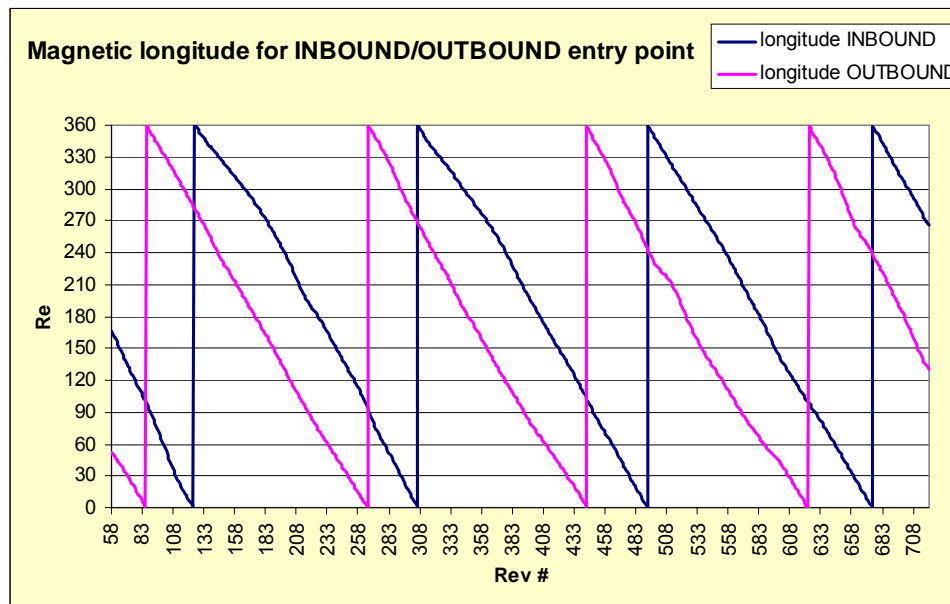


Figure 25 – magnetic longitude (SM system) evaluated from real RM data for both INBOUND and OUTBOUND legs

7.1.3 Basic concept for defining the “radiation surface”

Due to the choice of the SM reference frame (see paragraph 7.1.1) the surface will necessarily have a certain degree of symmetry; for example we can already anticipate that it will have to be symmetric with respect to the magnetic equator (i.e. X-Y plane).

In addition, though not necessarily a surface of revolution because of the asymmetry of the magnetic field w.r.t. longitude, it will have to be defined as a pseudo-torus surface, being the size and the shape of the cross section to be determined for different longitudes (note that fig.16 can already give a preliminary idea of what we are looking for).

Since the Earth size (in the middle of the structure) is small compared with the size of the entire surface we can assume that our pseudo-torus surface is of type “horn” (i.e. internal hole of zero dimension). See fig.26 for a visualization.

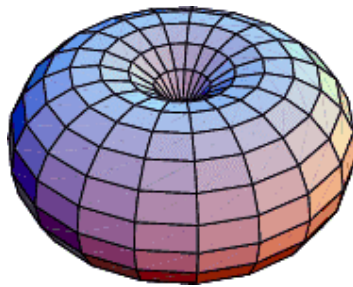


Fig. 26: horn-torus

From what has been said in paragraph 4.1.1, we can also assume that the part of the surface facing the sun direction (i.e. positive X) will be more extended (i.e. larger cross section) than the opposite part (facing the anti-sun direction). See fig.27 for a pictorial representation.

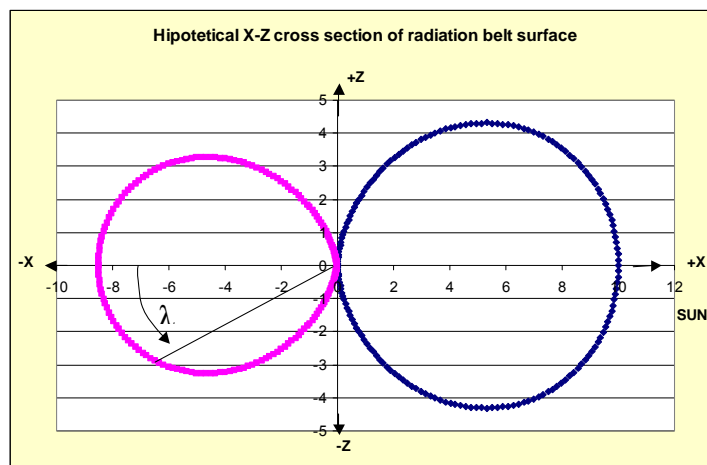


Figure 27 – potential cross-section on the X-Z plane of the “radiation surface” (see analogy with fig 16)

The shape and the size of the pseudo-torus cross-sections will be a function of the magnetic longitude. At a given longitude, the shape will of course imply a dependency on the latitude as well. The next paragraphs will concentrate on these aspects.

7.2 Determination of “radiation surface” size and shape

7.2.1 How to get some hints about the surface size

Projecting the foot print of the “real” surface at different latitudes (i.e. by plotting Y versus X for the real RAD_MON data shown in fig. 20 to 23 for different ranges of magnetic latitude) we obtain what displayed in fig. 28 (both inbound and outbound legs together).

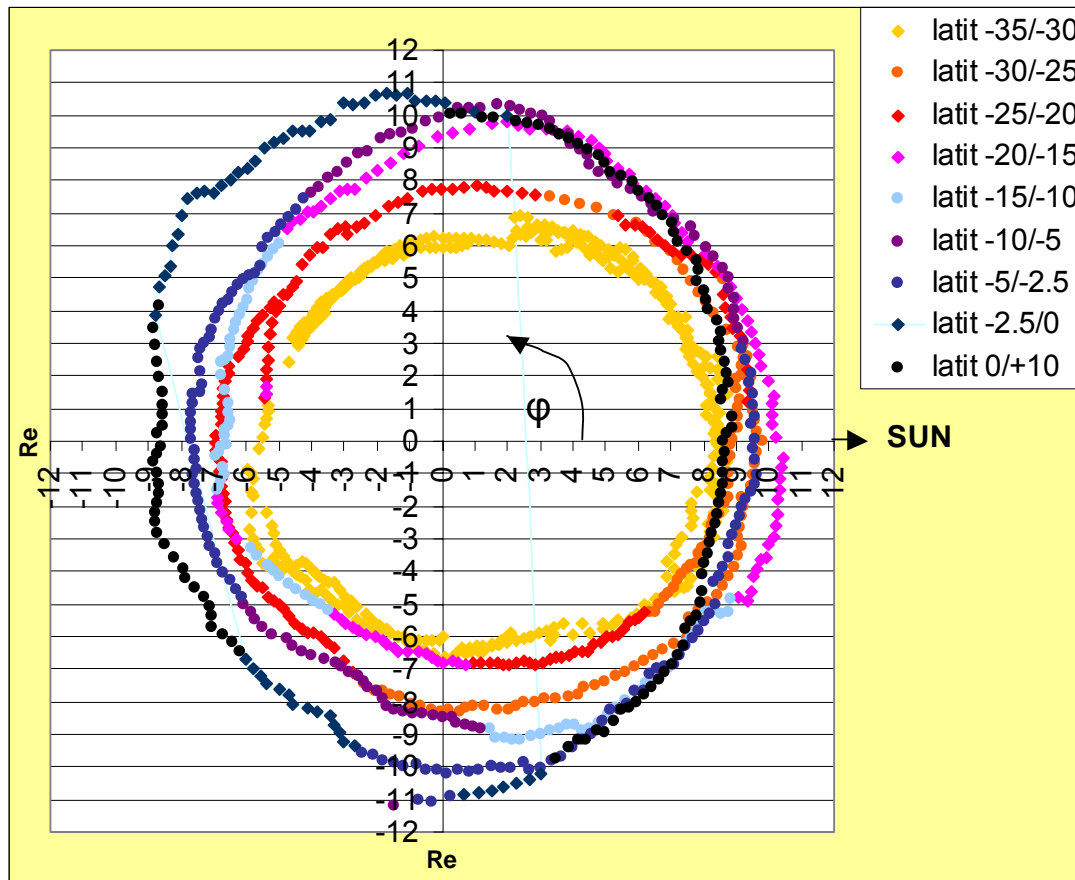


Figure 28 – Foot-prints of the “radiation surface” for different magnetic latitude ranges (obtained from Rad_Mon real data)

We can see that:

- The size is decreasing for increasing latitude (as obviously expected)
- For latitude < -15 deg, there is a significant asymmetry between the sunward side (+ X) and the anti-sun side (-X), as expected from the geometry of the Earth magnetic field (see paragraph 4.1.1).
- On the transversal axis (+ Y , -Y) the size is in general intermediate between + X (maximum) and - X (minimum)
- At least four parameters are needed to mathematically represent the size; these will be called from now on:
 - L1 = size of the + X side (Sunwards)
 - L2 = size of the - X side (Anti-Sun)
 - L_{y+} = size of the + Y side (transversal)
 - L_{y-} = size of the - Y side (transversal)
- For latitude in the approximate range $-10 \text{ deg} < \lambda < +10$ the asymmetry between the various sides of the surface (+ X, - X, + Y, -Y) is not so evident as for higher latitudes; we can in fact appreciate a significant expansion of the -X, +Y, -Y sides, while the sunward side remains basically unchanged (actually slightly reduced), in such a way that the projection on the plane of the global surface is getting closer to a circle. This is a very important point since it explains why for the INBOUND leg the seasonal effect seems to vanish as of REV-370 onwards. In fact, by looking at fig. 24, it can be seen that after Rev-370 the entry latitude is always in the range ± 10 deg (i.e. close to the magnetic equator); combining this with the fact that for latitude around zero the values of L1, L2, L_{y+} , L_{y-} are almost equivalent (or at least the differences are not so significant as it happens for higher latitudes), we can understand both the change in periodicity since now the +Y and -Y sides act as maximums as well (see fig 21) and the fact that the gap between the maximums and minimums of the curve shown in fig. 1 is not as pronounced as before Rev-370. Though we do not have a theoretical explanation for this, it is believed to be related to the structure and physics of the Neutral sheet and Plasma sheet regions (see fig 8).

What above also suggests that at least for the - X, + Y, - Y sides the expression of L_2 , L_{y+} , L_{y-} is actually latitude dependent. A suitable expression could be of the form:

$$\begin{aligned}
 L_2 &= L_{20} + \frac{\Delta L_{20}}{(a_2)^2} \cdot \left[\frac{\sin(a_2 \cdot \lambda)}{\lambda} \right]^2 \\
 L_{y+} &= L_{y+0} + \frac{\Delta L_{y+}}{(a_3)^2} \cdot \left[\frac{\sin(a_3 \cdot \lambda)}{\lambda} \right]^2 \\
 L_{y-} &= L_{y-0} + \frac{\Delta L_{y-}}{(a_4)^2} \cdot \left[\frac{\sin(a_4 \cdot \lambda)}{\lambda} \right]^2
 \end{aligned}
 \tag{eq-1}$$

where L_{20} , ΔL_2 , a_2 , etc. are parameters which have been determined by best fitting with experimental data:

	L	ΔL	a
L_2	6.7	2.6	20
L_{y+}	7.8	3.4	6
L_{y-}	9.0	2.8	20

See also picture 28-B for a visualization.

As it can be seen from fig. 28, the maximum extension on the sunward side (+ X) is reached instead at a latitude close to -14 deg. (reason for this is unknown). Relevant expression for L_1 is provided here below (see also fig 28-C):

$$L_1 = L_{10} + \frac{\Delta L_{10}}{(a_1)^2} \cdot \left[\frac{\sin(a_1 \cdot (\lambda + 14^\circ))}{(\lambda + 14^\circ)} \right]^2 \quad (\text{eq. 1-b})$$

with values:

	L	ΔL	a
L_1	8.9	1.3	50

In order to insure the continuity of the surface as a function of longitude we need to impose the following relations:

$$\begin{aligned} \text{for } 180 \leq \varphi \leq 270: & \quad L_p = L_y - (L_y - L_2) \cdot \cos(\varphi) \\ \text{for } 270 \leq \varphi \leq 360: & \quad L_p = L_1 + (L_1 - L_{y-}) \cdot \sin(\varphi) \\ \text{for } 0 \leq \varphi \leq 90: & \quad L_p = L_y + (L_1 - L_{y+}) \cdot \cos(\varphi) \\ \text{for } 90 \leq \varphi \leq 180: & \quad L_p = L_y + (L_y - L_2) \cdot \cos(\varphi) \end{aligned} \quad (\text{eq. 2})$$

L_p defined here above (eq. 1, 1-b & 2) can be interpreted as the measure of the surface size as function of magnetic latitude and longitude (i.e. where the surface envelope passing through a point identified by λ and φ would cross the magnetic equator).

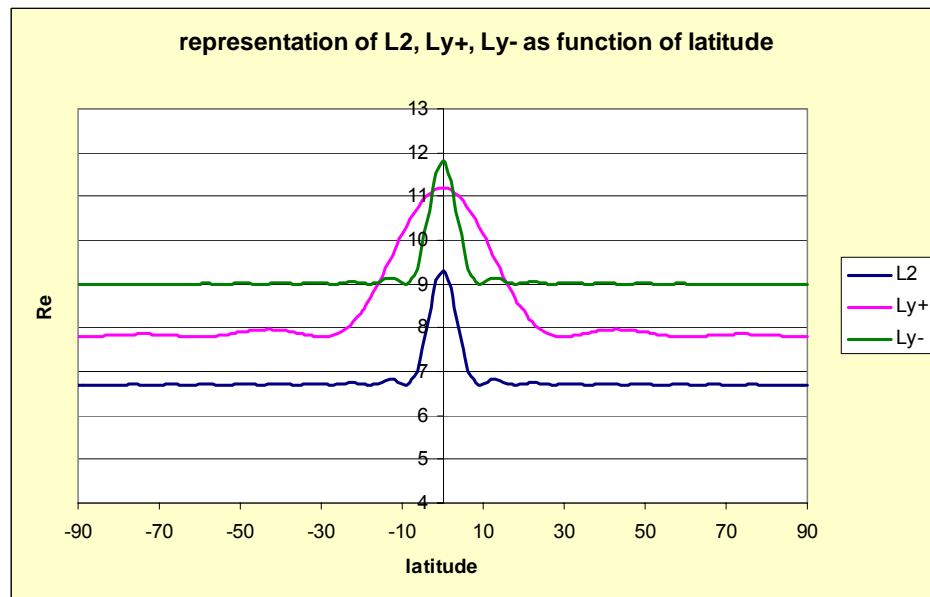


Figure 28-B – graphical representation of L_2 , L_{y+} , L_{y-} as a function of magnetic latitude

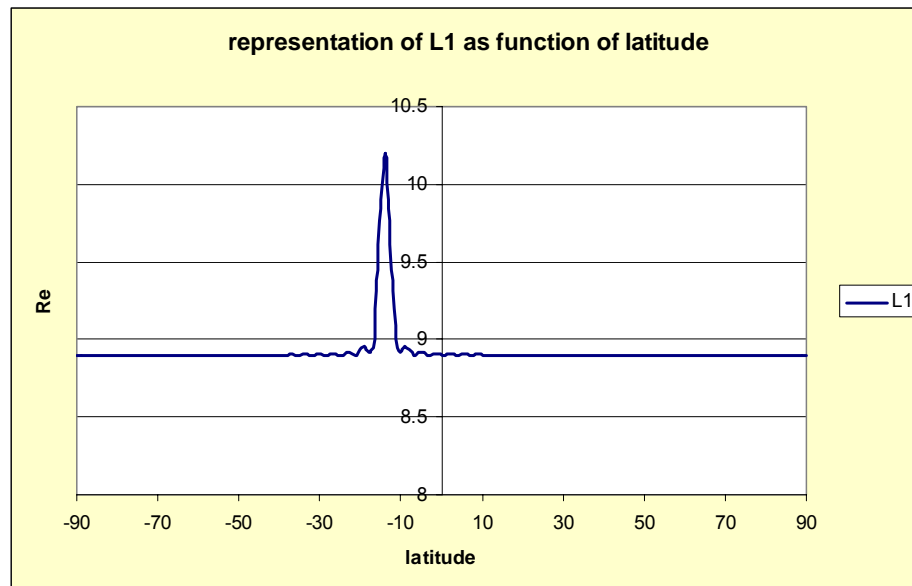


Figure 28-C – graphical representation of L_1 as a function of magnetic latitude

7.2.2 How to get some hints about the surface shape

By considering a dipolar magnetic field line (see fig. 29 and 30) the relevant equation in polar coordinates can be written as:

$$r = L \cdot \cos^2(\lambda) \quad (\text{note that } r \text{ is expressed in Earth radii}) \quad (\text{eq. 3})$$

where L is the distance, expressed in Earth radii, where the field line intersects the magnetic equator. On the other hand the dipolar magnetic field intensity along a field line is given by:

$$B = \frac{B_0}{L^3} \cdot \sqrt{1 + 3 \cdot \sin^2(\lambda)} \quad (\text{eq. 4})$$

where B_0 is the equatorial field at the Earth surface. If B_{\min} is now the minimum magnetic field intensity on the magnetic equator for trapping particles, then the same value of B_{\min} for $|\lambda| > 0$ is reached at distances which are greater by a factor:

$$\sqrt[6]{1 + 3 \cdot \sin^2(\lambda)} \quad (\text{eq. 5})$$

This means that for $|\lambda| > 0$, we can expect a contribution from different drift shells (i.e. from particles linked to more distant magnetic field lines). The shape of the surface cross-section is therefore expected to significantly deviate from the shape of a single magnetic field line (i.e. getting “fatter” with respect to the curve depicted in fig. 30, which is equivalent of lowering the exponent in equation 3).

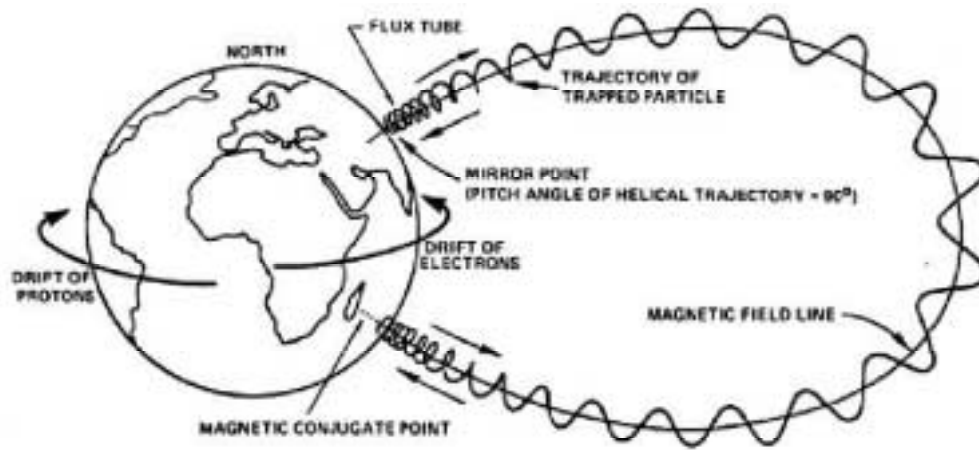


Figure 29 – representation of an Earth dipolar magnetic field line with trapped particles

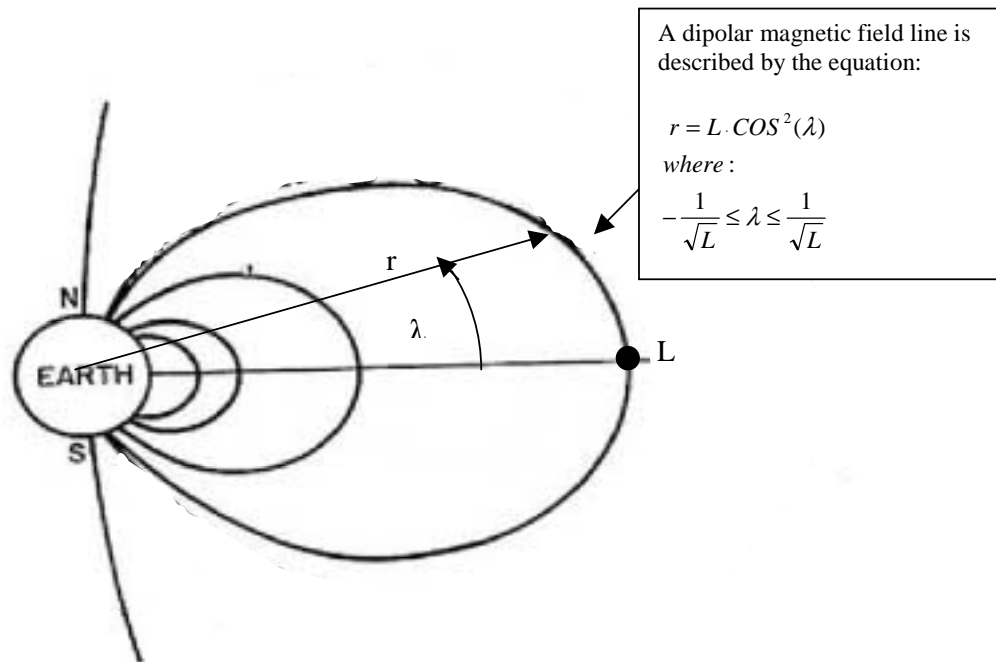


Figure 30 – Geometrical representation and mathematical expression of a dipolar magnetic field line

Since the field we are actually considering is not dipolar, in the most general way we could write the equation of a surface cross-section at a given longitude as:

$$r = L_p(\lambda, \varphi) \cdot \sqrt[6]{(1 + K(\varphi) \cdot \sin^2(\lambda) \cdot \cos^{j(\varphi)}(\lambda))} = f(\lambda, \varphi) \quad (\text{eq. 6})$$

In the above expression, $L_p(\lambda, \varphi)$ is given by the equations 1 & 2. The pending job is now to determine $K(\varphi)$, $j(\varphi)$ in equation 6 by comparison and best-fitting mechanisms w.r.t. experimental data. In order to reduce the number of unknowns we may impose:

$$j(\varphi) = \frac{7}{4} - \frac{1}{4} \cdot \cos(\varphi) \quad (\text{eq. 7})$$

which implies $j = 2$ for the anti-sun side and $j = 1.5$ for the sunward side and varying with continuity between the two extremes, as shown in fig 31.

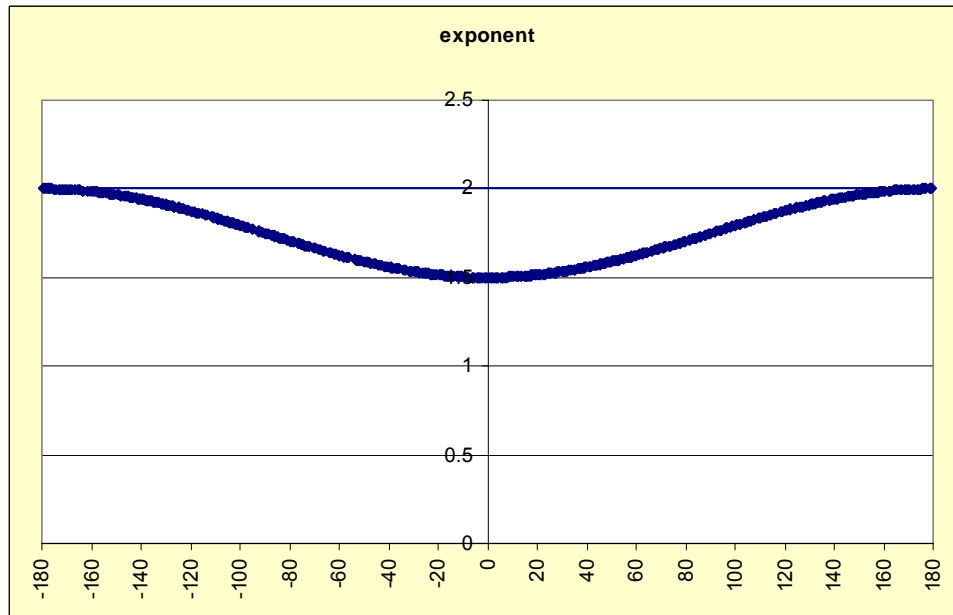


Figure 31 – Graphical representation of $j(\varphi)$, i.e. exponent of $\cos(\lambda)$ in equation 6 above

Though this imposition can look slightly arbitrary, it has to be taken into account that any error on $j(\varphi)$ as per above assumption will anyhow be compensated in the expression of $K(\varphi)$.

$K(\varphi)$ has been determined empirically by best-fit with real data and is given by equation:

$$K(\varphi) = 27 \cdot \cos^2(\varphi) + 7.5 \cdot \sin^2(\varphi) + 4.5 \cdot \sin(\varphi) + 10 \cdot \cos(\varphi) \quad (\text{eq. 8})$$

This is visualized in fig. 32.

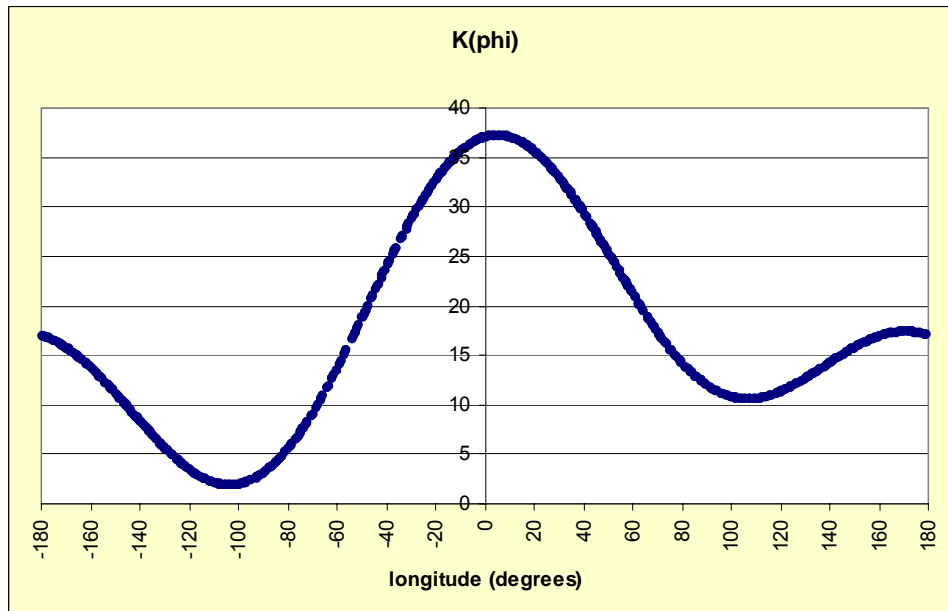


Figure 32 – Graphical representation of $K(\varphi)$ (see eq. 6 & 8)

7.3 Final equations and model results

7.3.1 Mathematical equations

As presented in paragraph 7.2.2 a cross-section of our surface for a given longitude φ can be expressed by the equation in polar coordinates:

$$r = L_p(\lambda, \varphi) \cdot \sqrt[6]{(1 + K(\varphi) \cdot \sin^2(\lambda) \cdot \cos^{j(\varphi)}(\lambda))} = f(\lambda, \varphi) \quad (\text{eq. 6})$$

Taking into account what said in paragraph 7.1.3, the whole surface will therefore be represented by the following equations in spherical coordinates:

$$\begin{aligned} X(\lambda, \varphi) &= r \cdot \cos(\lambda) \cdot \cos(\varphi) = f(\lambda, \varphi) \cdot \cos(\lambda) \cdot \cos(\varphi) \\ Y(\lambda, \varphi) &= r \cdot \cos(\lambda) \cdot \sin(\varphi) = f(\lambda, \varphi) \cdot \cos(\lambda) \cdot \sin(\varphi) \\ Z(\lambda, \varphi) &= r \cdot \sin(\lambda) = f(\lambda, \varphi) \cdot \sin(\lambda) \end{aligned} \quad (\text{eq. 9})$$

i.e.:

$$\begin{aligned} X(\lambda, \varphi) &= L_p(\lambda, \varphi) \cdot \sqrt[6]{(1 + K(\varphi) \cdot \sin^2(\lambda) \cdot \cos^{j(\varphi)+1}(\lambda))} \cdot \cos(\varphi) \\ Y(\lambda, \varphi) &= L_p(\lambda, \varphi) \cdot \sqrt[6]{(1 + K(\varphi) \cdot \sin^2(\lambda) \cdot \cos^{j(\varphi)+1}(\lambda))} \cdot \sin(\varphi) \\ Z(\lambda, \varphi) &= L_p(\lambda, \varphi) \cdot \sqrt[6]{(1 + K(\varphi) \cdot \sin^2(\lambda) \cdot \cos^{j(\varphi)}(\lambda))} \cdot \sin(\lambda) \end{aligned} \quad (\text{eq. 10})$$

where:

L_p is as per equations 1, 1-b & 2; numerical values for L_1 , L_2 , L_{y+} , L_{y-} , a_1 , a_2 , etc. were determined by comparison with real data (min-squares method).

$j(\varphi)$: as per equation 7

$K(\varphi)$: as per equation 8

7.3.2 Model results

By feeding the latitude and longitude values derived from the real data (see fig 24 & 25) into equations 10 we may evaluate the X-Y-Z coordinate values predicted by the model for both the inbound and outbound legs.

The comparison between the model outputs and the real data is provided in fig 33 to 36 (inbound) and in fig 39 to 42 (outbound) respectively. The differences between model and real data are shown in fig. 37 & 38 (inbound) and in fig 43 & 44 (outbound).

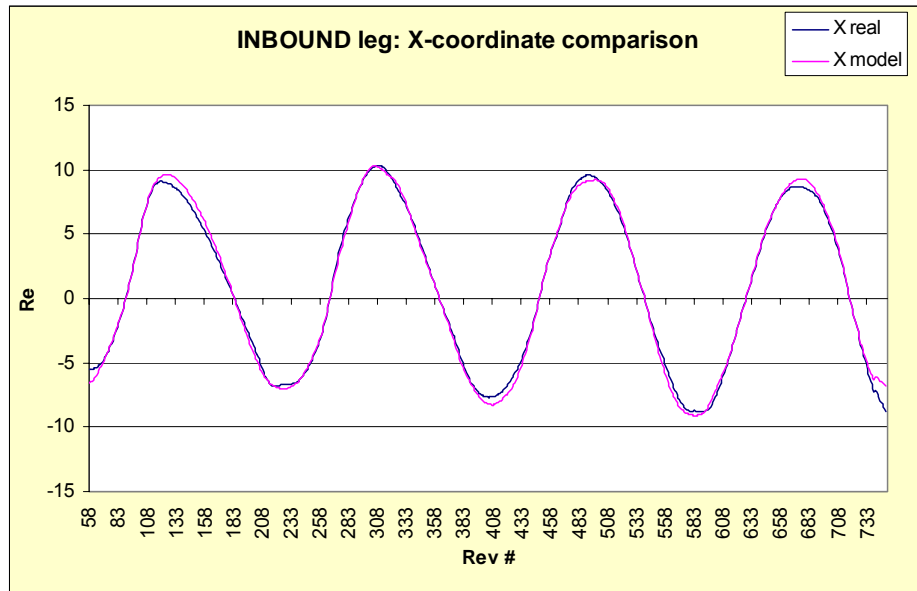


Figure 33 – INBOUND leg: comparison of X-coordinates (model versus real data)

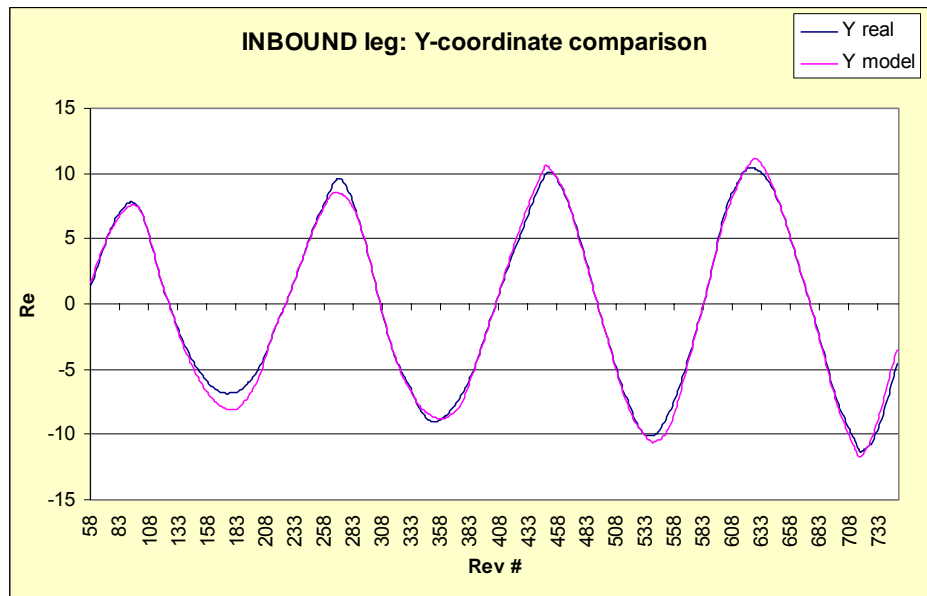


Figure 34 – INBOUND leg: comparison of Y-coordinates (model versus real data)

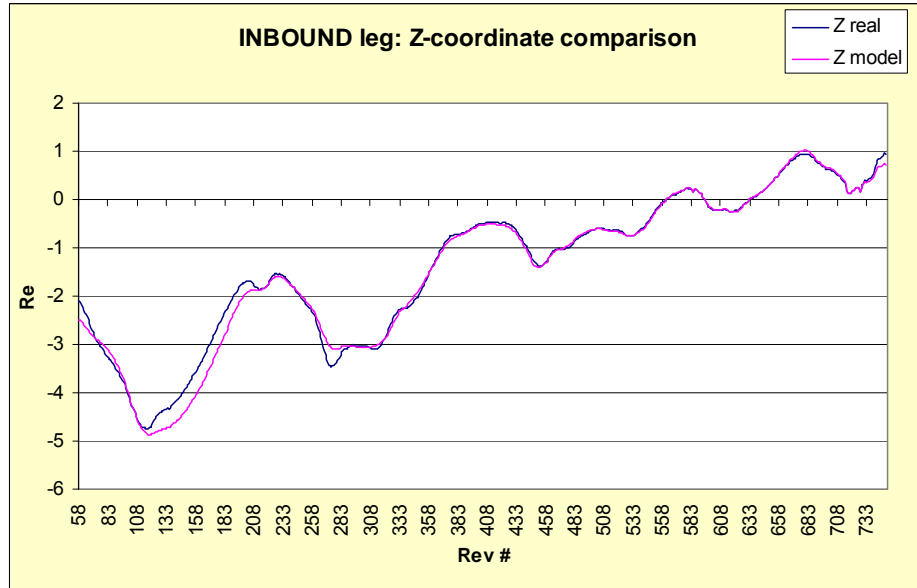


Figure 35 – INBOUND leg: comparison of Z-coordinates (model versus real data)

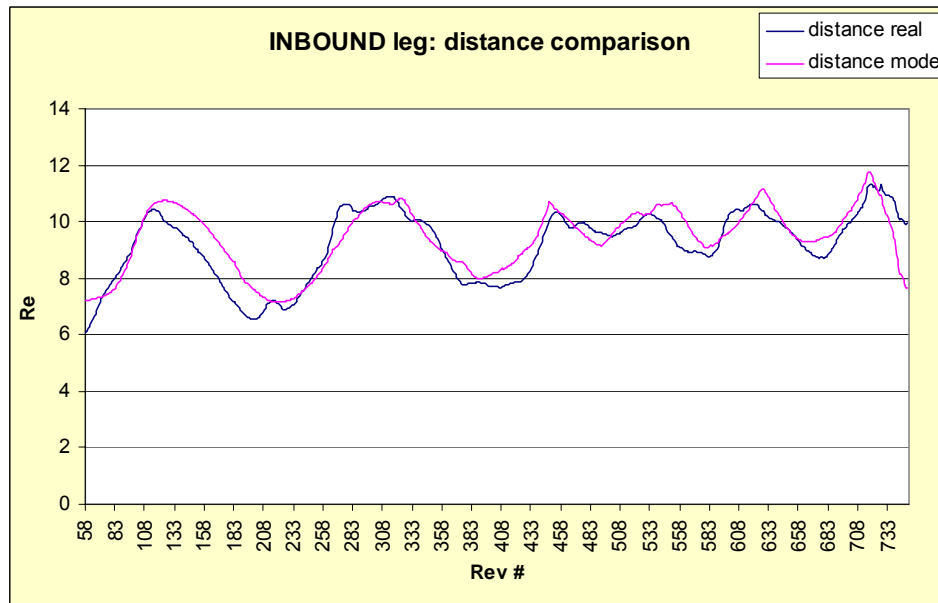


Figure 36 – INBOUND leg: comparison of distance (model versus real data)

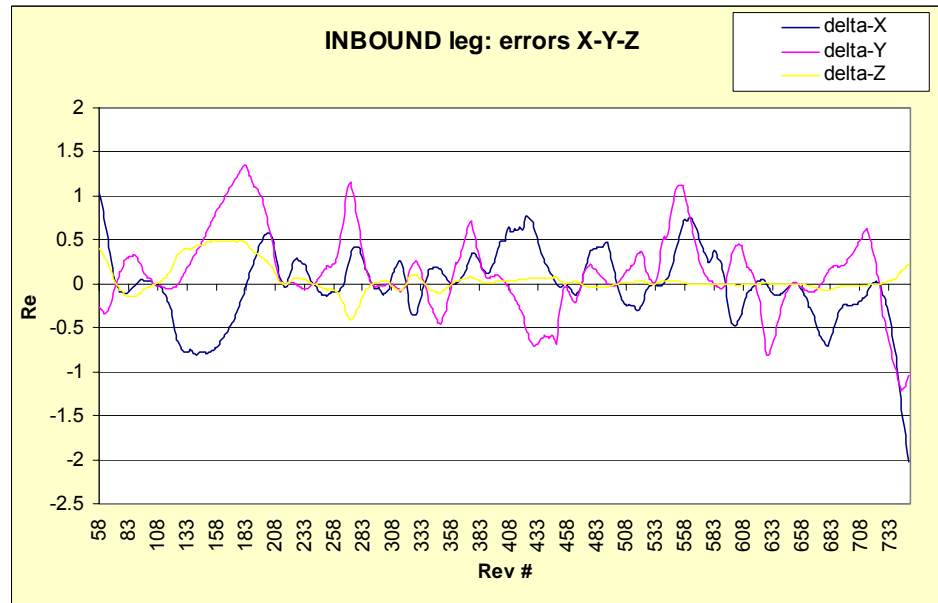


Figure 37 – INBOUND leg: visualization of $\Delta X / \Delta Y / \Delta Z$

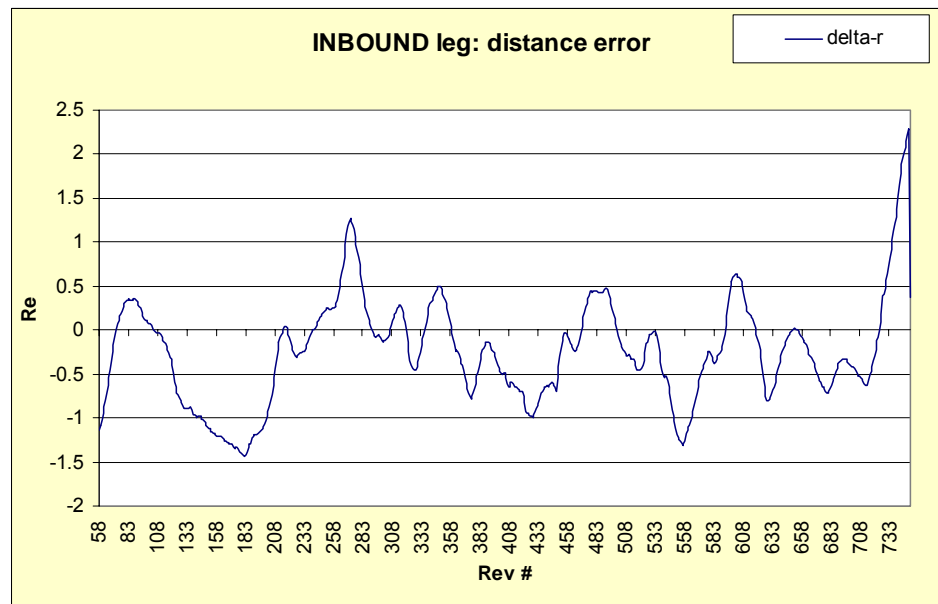


Figure 38 – INBOUND leg: visualization of Δr

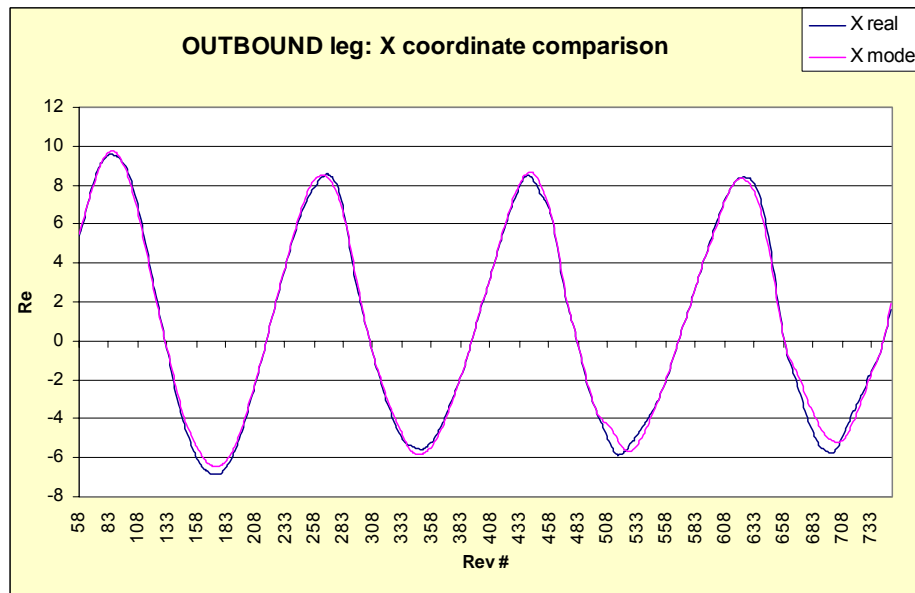


Figure 39 – OUTBOUND leg: comparison of X-coordinates (model versus real data)

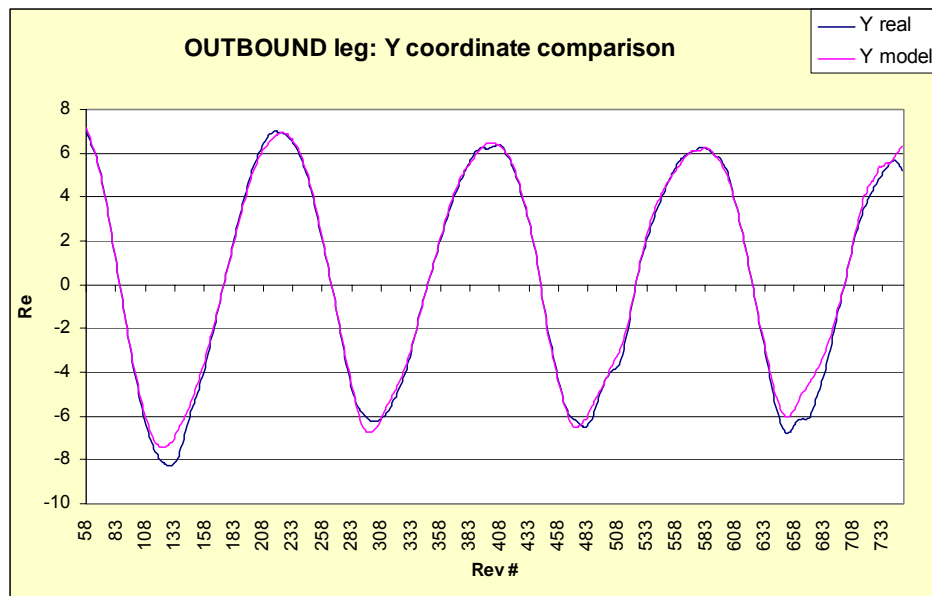


Figure 40 – OUTBOUND leg: comparison of Y-coordinates (model versus real data)

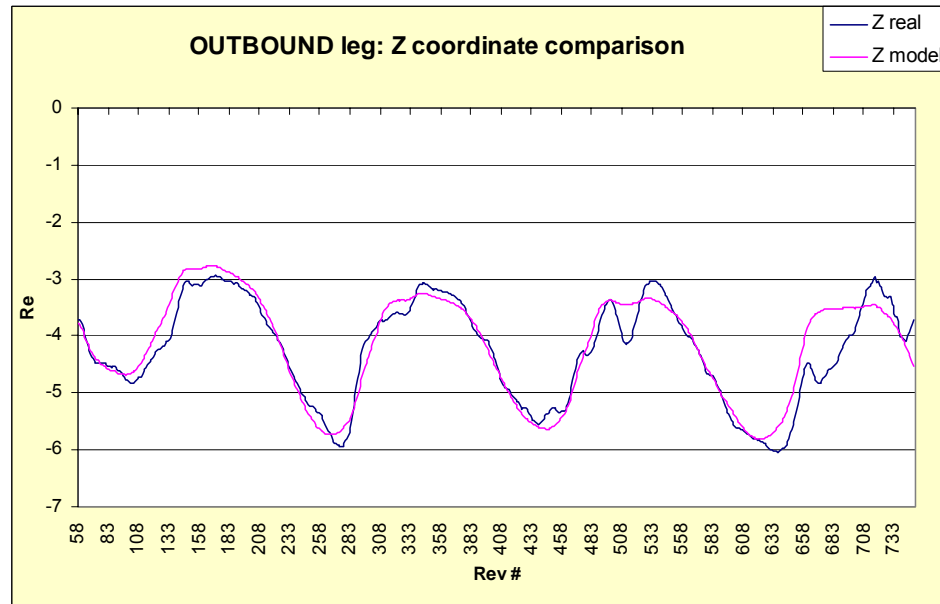


Figure 41 – OUTBOUND leg: comparison of Z-coordinates (model versus real data)

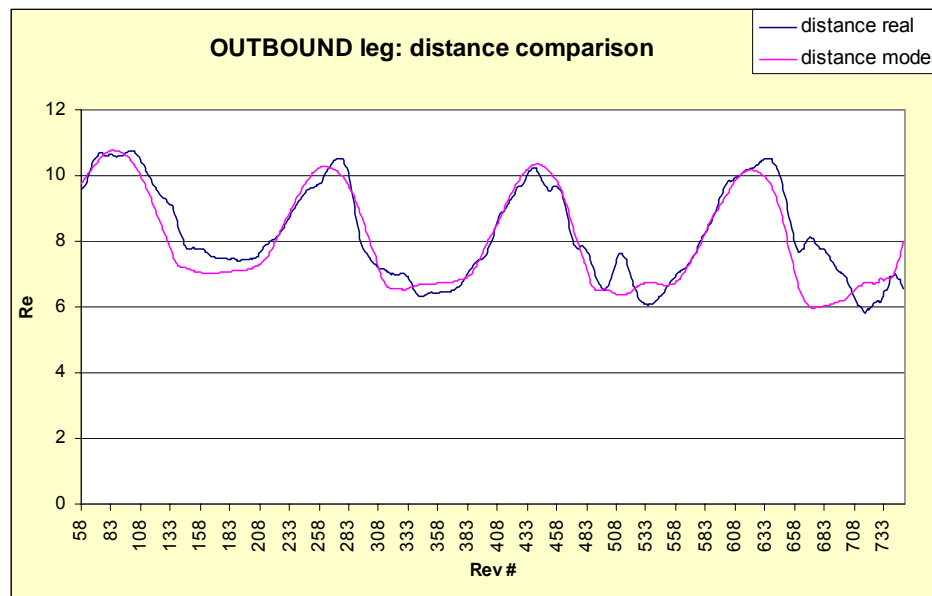


Figure 42 – OUTBOUND leg: comparison of distance (model versus real data)

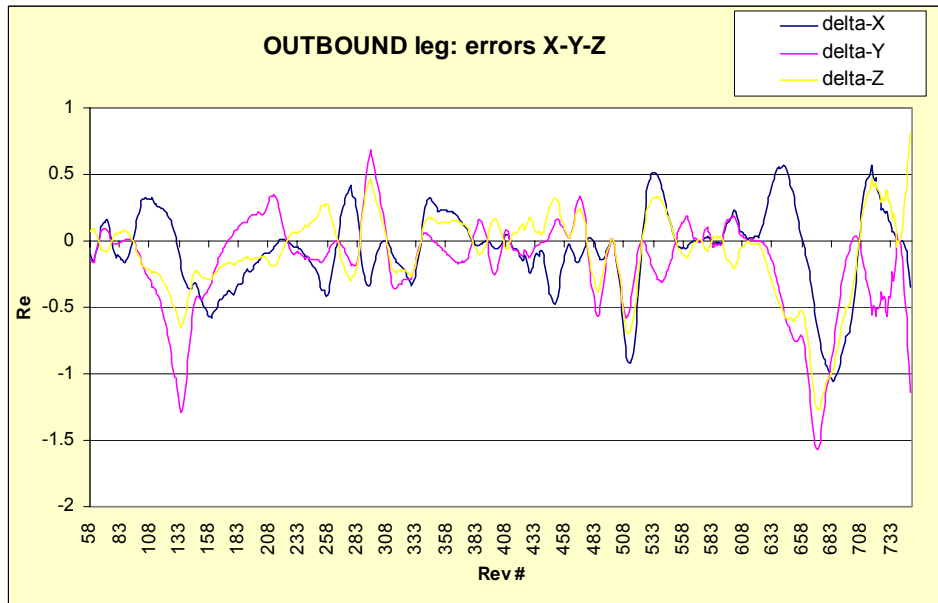


Figure 43 – OUTBOUD leg: visualization of ΔX / ΔY / ΔZ

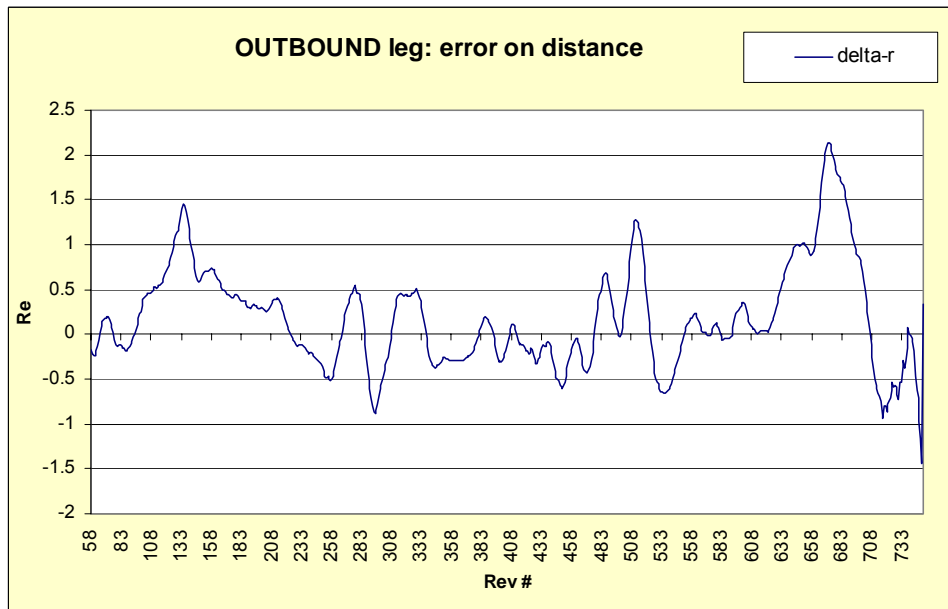


Figure 44 – OUTBOUND leg: visualization of Δr

7.3.3 Model algorithm

All the processing is based on the XMM Orbit File “ORBITA” periodically produced by the XMM Flight Dynamics team. This contains: reconstructed orbit (from ranging data) for the whole past mission and predictions for about one year into the future (based on estimate of orbit perturbations).

The model is based on the following user’s inputs:

1. range of revolutions to be processed (can be in the past or in the future, provided they are in the Orbit file range of validity)
2. Integration step for the orbit evaluation (normally between 1 and 10 min)
3. Integration window per orbit (normally between perigee –12 h and perigee + 12 h)

The model algorithm consists of the following main steps:

a) for each orbit in the selected range (as per input 1 above) evaluate the spacecraft position with a resolution given by input 2 above and for the period specified by input 3. At each step the following is done:

- By using the orbit file determine the spacecraft coordinates in the Inertial reference system
- Transform the spacecraft coordinates into the SM system by using the Tsyganenko-2001 Earth magnetic field model
- Evaluate from the spacecraft coordinates in the SM system (from previous step) the magnetic longitude and latitude and the spacecraft distance
- Feed magnetic longitude and latitude into equations 10 and evaluate the surface coordinates
- Evaluate the surface envelope (i.e. extension) at that point (i.e. $\text{SQRT}(X_{\text{surf}}^2 + Y_{\text{surf}}^2 + Z_{\text{surf}}^2)$)
- Compare the spacecraft distance with the surface envelope and determine whether inside or outside the surface
- If inside set flag WF=ACTIVE, if outside set flag WF=INACTIVE

b) repeat all above steps for all points inside the specified window (e.g. between perigee – 12 h and perigee + 12 h)

c) repeat for all revolutions selected by the user

d) scan for all revolutions the flag status and identify transitions

e) associate absolute time to above transitions

f) present data to user in file and graphical formats

7.3.4 Model outcomes

The outcomes of the model for the revolutions in the range 58-700 are presented in fig 45 to 47. A comparison between model outputs and RM data (not smoothed) is provided in fig. 48 & 49. The delta-time between real data and model outputs is shown in fig. 50 to 53; it has been evaluated and displayed for both the smoothed data (see fig 13 & 14) and the RM genuine data (see fig 1 & 2). The accuracy of the model is summarized in the table below:

comparison with smoothed RM data	mean error (hours)	standard deviation (h)	max error (abs. Value in hours)
OUTBOUND leg	-0.16	0.38	1.42
INBOUND leg	0.09	0.39	1.15
comparison with genuine RM data (flares removed)	mean error (hours)	standard deviation (h)	max error (abs. Value in hours)
OUTBOUND leg	-0.19	1.05	4.6
INBOUND leg	0.09	1.02	4.2

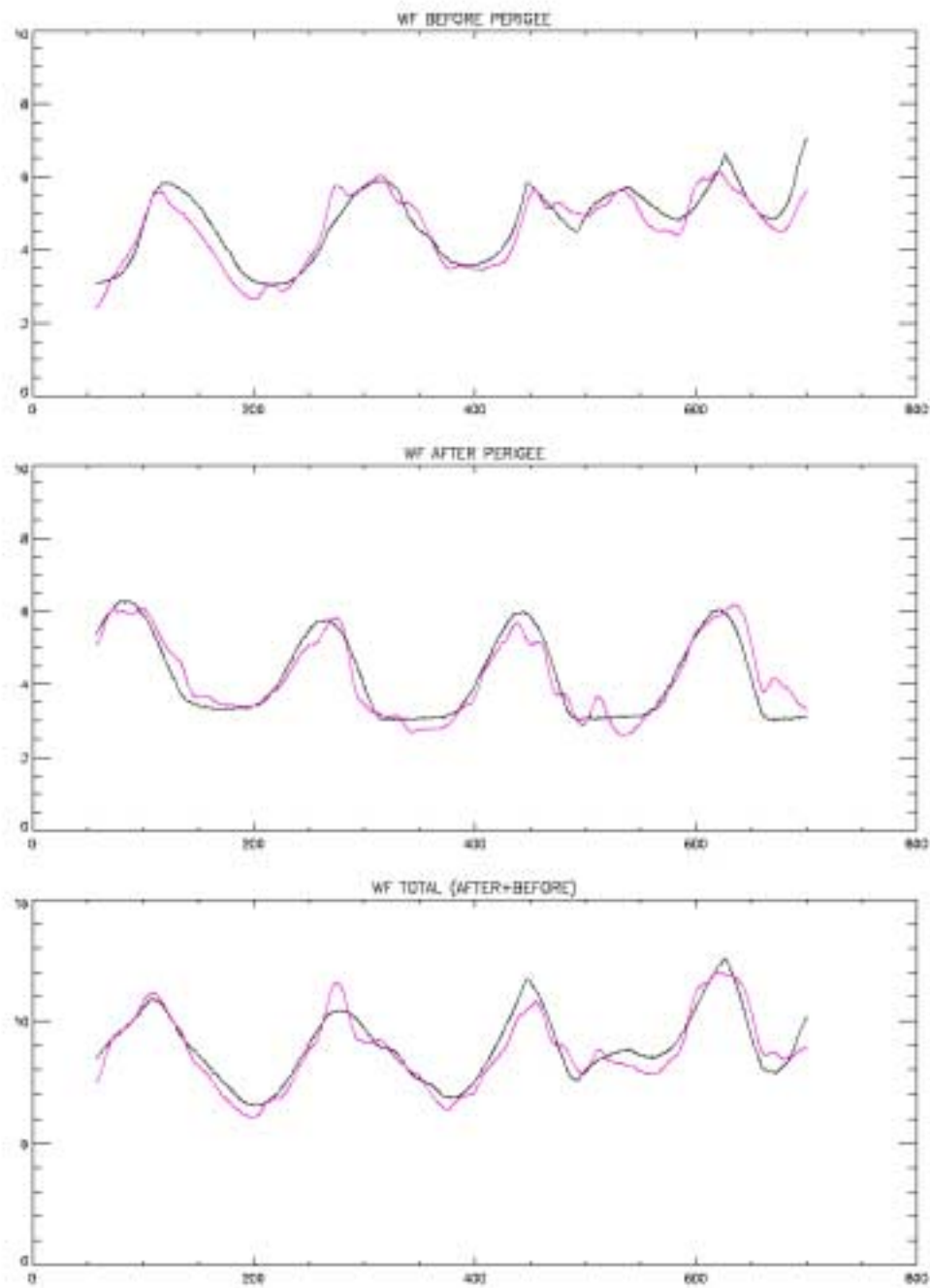


Figure 45 – comparison of predicted and actual time for inbound leg, outbound leg and total radiation belt crossing time (real data are in red, model data in black)

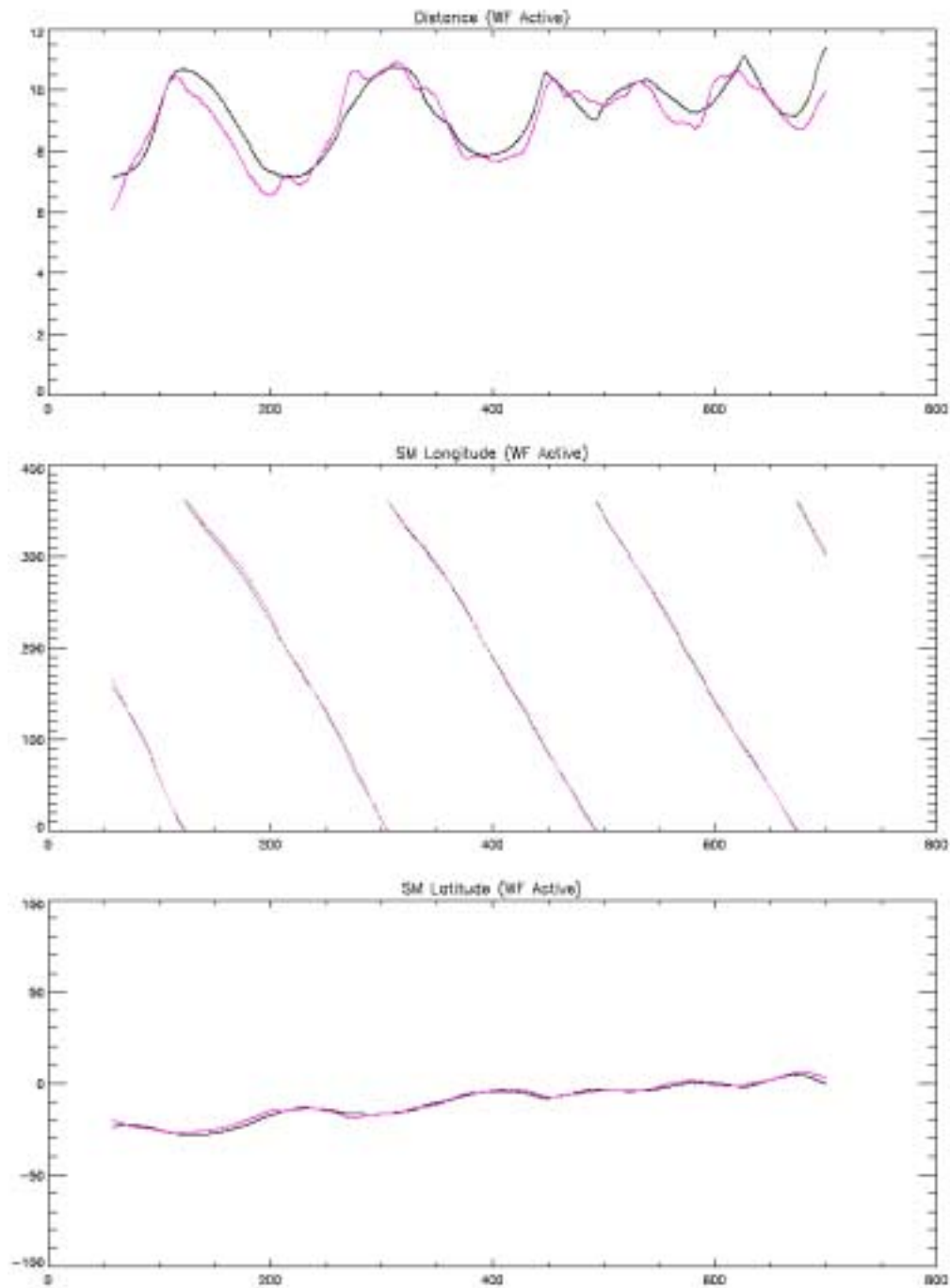


Figure 46 – INBOUND leg: comparison of predicted and actual distance, longitude and latitude of the radiation belts entry point (real data are in red, model data in black)

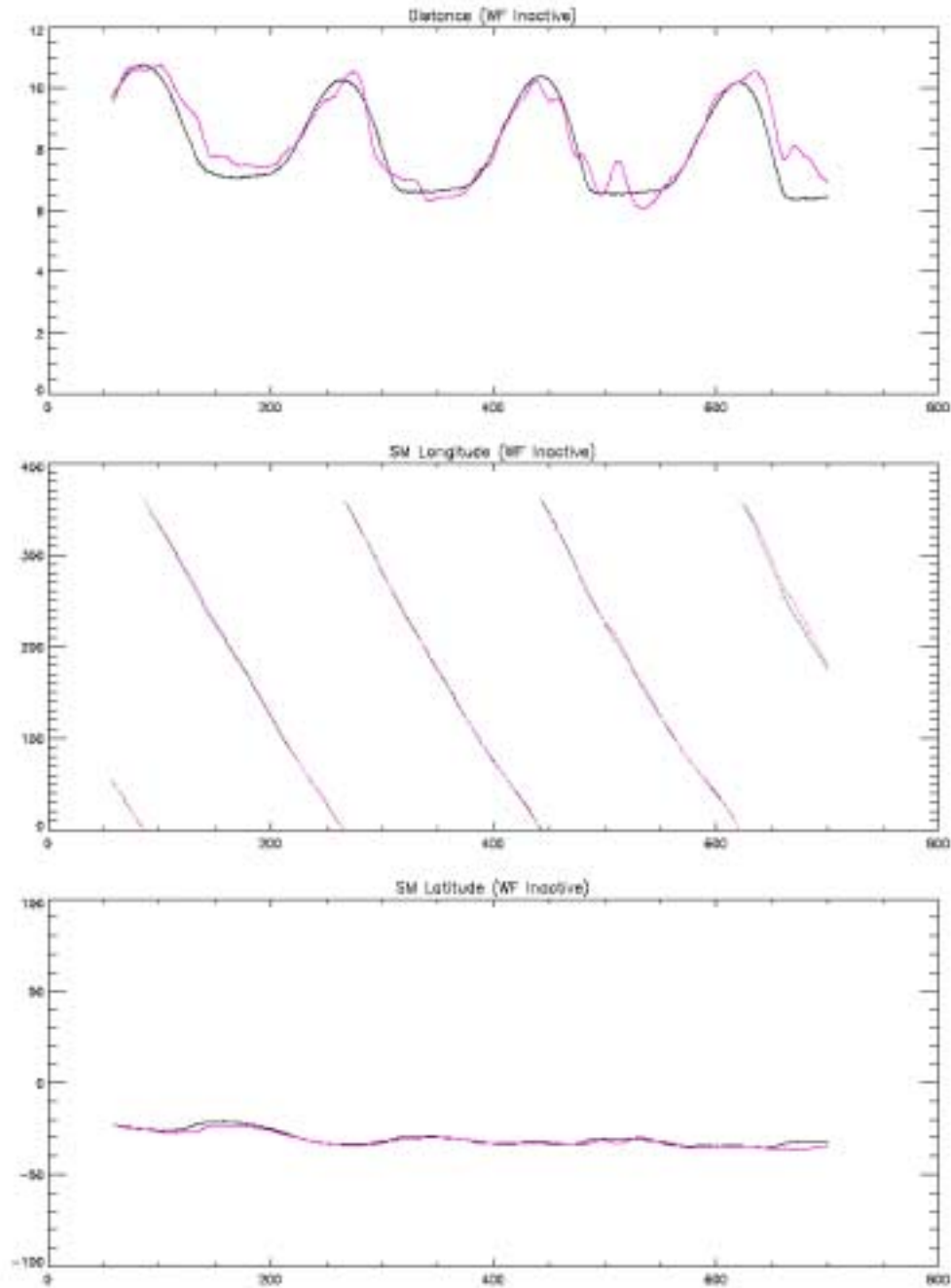


Figure 47 – OUTBOUND leg: comparison of predicted and actual distance, longitude and latitude of the radiation belts exit point (real data are in red, model data in black)

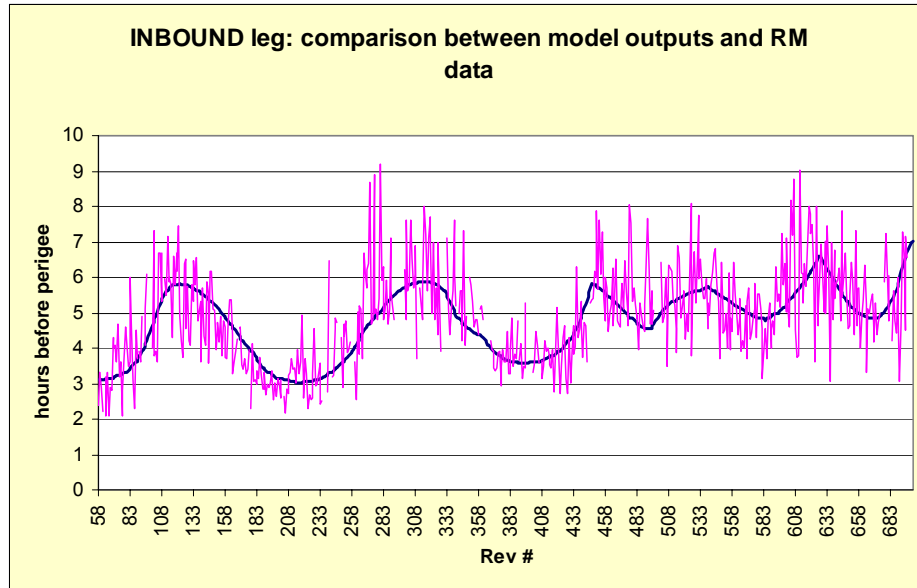


Figure 48 – INBOUND leg: comparison between model outputs and RM data (not smoothed)

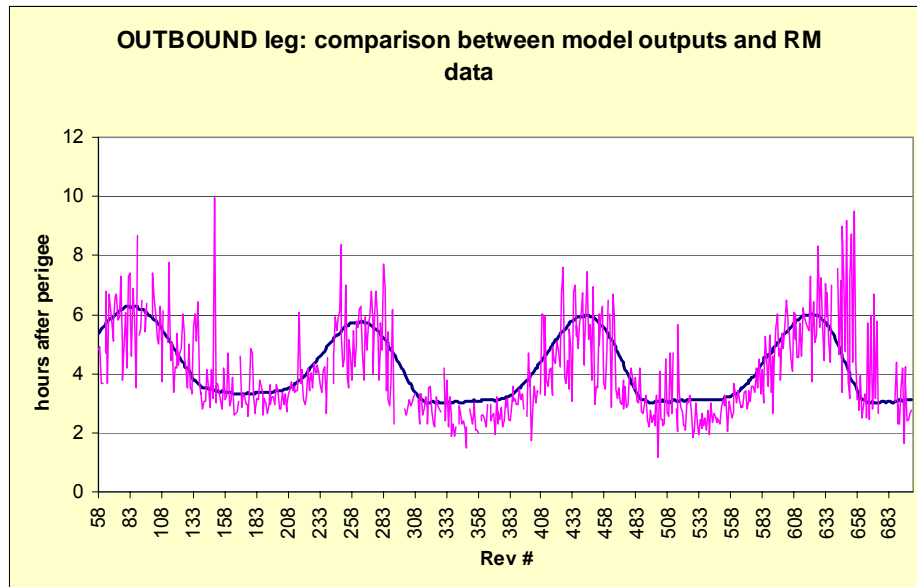


Figure 49 – OUTBOUND leg: comparison between model outputs and RM data (not smoothed)

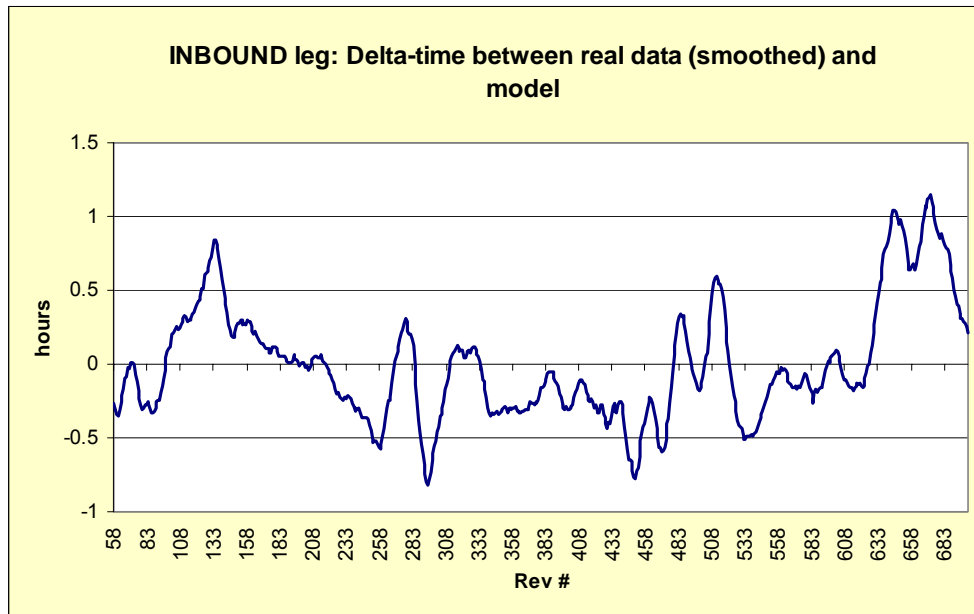


Figure 50 – INBOUND leg: visualization of Δ time w.r.t. smoothed curve

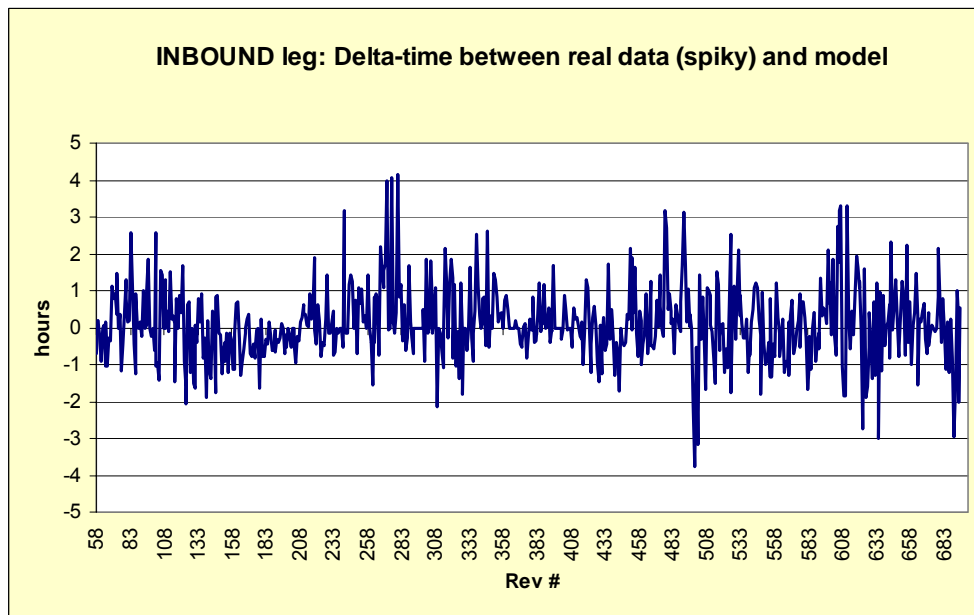


Figure 51 – OUTBOUND leg: visualization of Δ time w.r.t. spiky curve

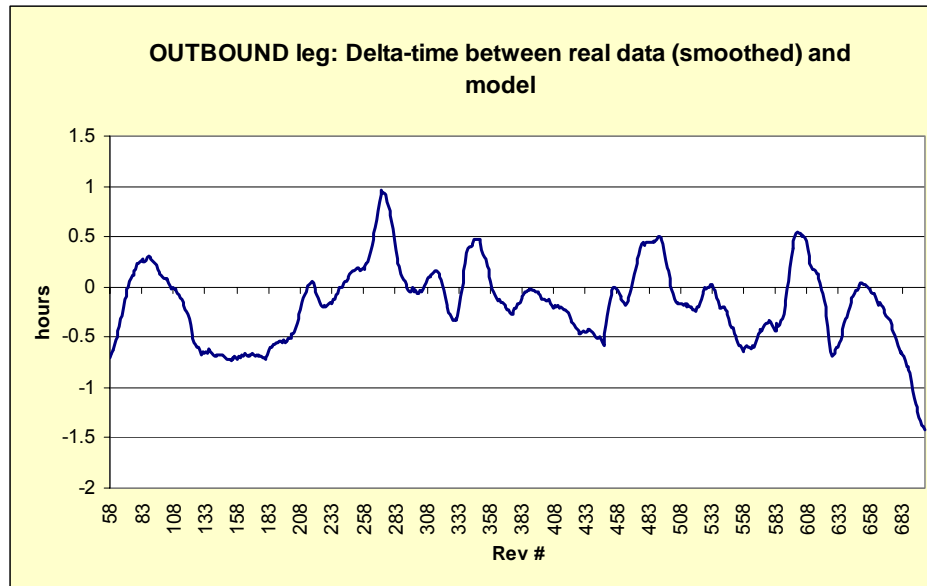


Figure 52 – OUTBOUND leg: visualization of Δ time w.r.t. smoothed curve

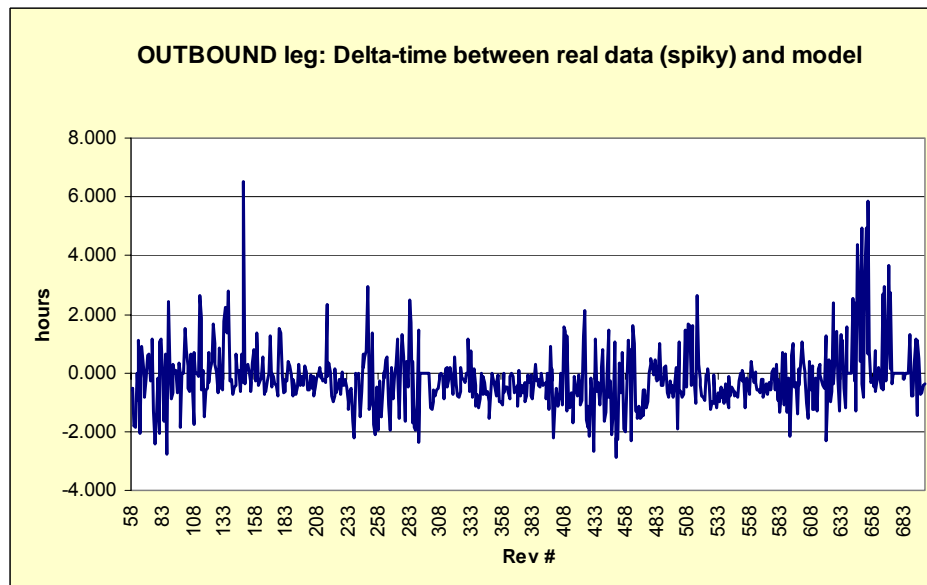


Figure 53 – OUTBOUND leg: visualization of Δ time w.r.t. spiky curve

7.3.5 Model predictions (next 90 revolutions)

The model predictions for the next 90 revolutions (from Rev 761 to 850) are provided in fig. 54 (tabular format) and in fig 55 & 56 for the pre-perigee and post-perigee paths, respectively.

REV	WF-AC	WF-IN	REV	WF-AC	WF-IN
761	-3.33333	4.33333	806	-6.83333	5.66667
762	-3.33333	4.5	807	-6.83333	5.5
763	-3.33333	4.5	808	-6.66667	5.5
764	-3.33333	4.5	809	-6.66667	5.5
765	-3.33333	4.66667	810	-6.66667	5.33333
766	-3.33333	4.66667	811	-6.5	5.33333
767	-3.33333	4.66667	812	-6.5	5.33333
768	-3.33333	4.83333	813	-6.33333	5.16667
769	-3.33333	4.83333	814	-6.33333	5.16667
770	-3.33333	4.83333	815	-6.33333	5
771	-3.33333	5	816	-6.16667	5
772	-3.33333	5	817	-6.16667	4.83333
773	-3.33333	5	818	-6.16667	4.83333
774	-3.33333	5	819	-6	4.66667
775	-3.33333	5.16667	820	-6	4.5
776	-3.33333	5.16667	821	-6	4.5
777	-3.5	5.16667	822	-6	4.33333
778	-3.5	5.33333	823	-5.83333	4.16667
779	-3.5	5.33333	824	-5.83333	4.16667
780	-3.5	5.33333	825	-5.83333	4
781	-3.5	5.33333	826	-5.83333	3.83333
782	-3.5	5.5	827	-5.83333	3.83333
783	-3.66667	5.5	828	-5.83333	3.66667
784	-3.66667	5.5	829	-5.66667	3.66667
785	-3.66667	5.5	830	-5.66667	3.5
786	-3.66667	5.66667	831	-5.66667	3.5
787	-3.83333	5.66667	832	-5.66667	3.33333
788	-3.83333	5.66667	833	-5.66667	3.33333
789	-4	5.66667	834	-5.66667	3.16667
790	-4	5.66667	835	-5.66667	3.16667
791	-4	5.66667	836	-5.66667	3.16667
792	-4.16667	5.83333	837	-5.66667	3
793	-4.33333	5.83333	838	-5.66667	3
794	-4.33333	5.83333	839	-5.66667	3
795	-4.5	5.83333	840	-5.66667	3
796	-4.66667	5.83333	841	-5.66667	3
797	-4.66667	5.83333	842	-5.66667	3
798	-4.83333	5.83333	843	-5.66667	3
799	-5	5.83333	844	-5.66667	3
800	-5.33333	5.83333	845	-5.66667	3
801	-5.5	5.83333	846	-5.66667	3
802	-5.83333	5.66667	847	-5.66667	3
803	-6.16667	5.66667	848	-5.66667	3
804	-6.33333	5.66667	849	-5.66667	3
805	-6.66667	5.66667	850	-5.66667	3

Figure 54 – predictions for the next 90 revolutions (tabular format)

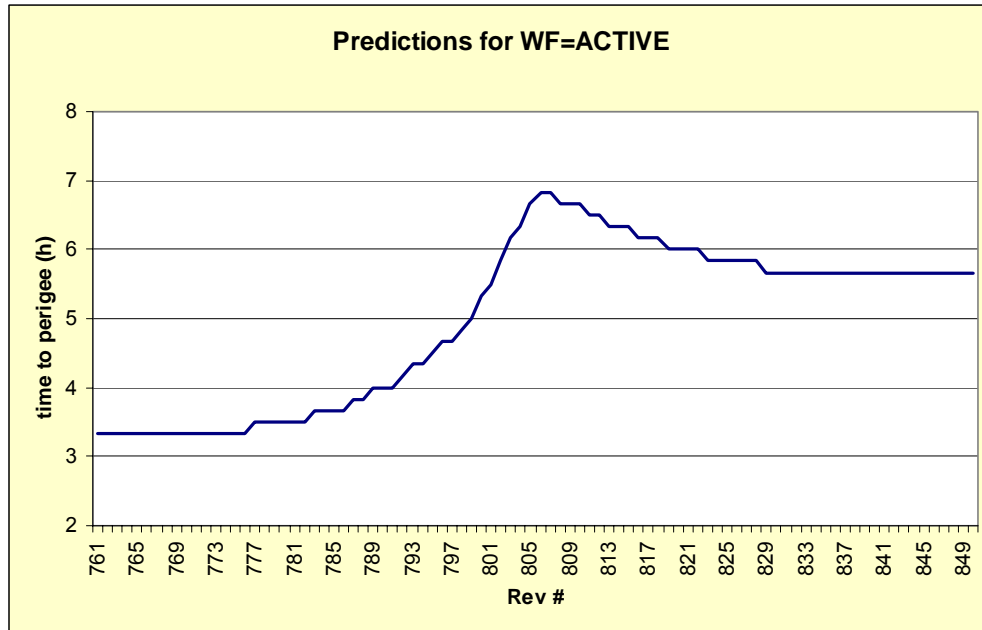


Figure 55 – predictions for the next 90 revolutions – Pre-Perigee

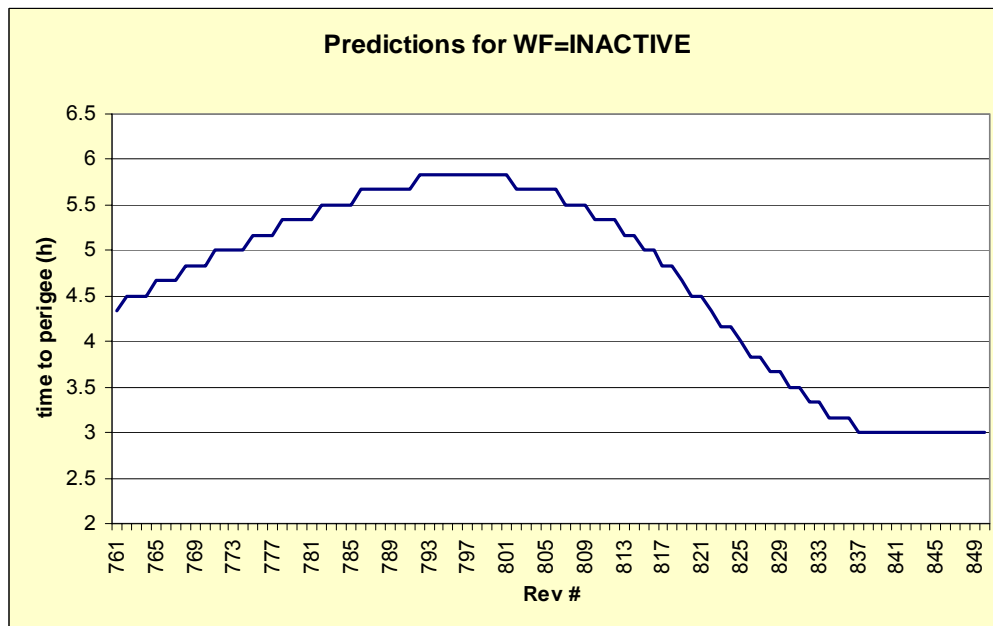


Figure 56 – predictions for the next 90 revolutions – Post-Perigee

Acknowledgments

This work would have not been possible without the excellent support and dedication of J. Fauste who has developed all the dynamical routines for Orbit file processing, reference frame transformation, etc. which are used within the model. He is also the author of the actual model code. We also acknowledge the support of M. Smith for an independent processing and graphical representation of the RM / RGS radiation data that constituted a great help for this work.